

On the Incidence and Kinematics of Strong Mg II Absorbers

Gabriel E. Prochter, Jason X. Prochaska

*Department of Astronomy and Astrophysics, University of California, 1156 High Street,
Santa Cruz, CA 95064*

prochter@ucolick.org, xavier@ucolick.org

and

Scott M. Burles

*Kavli Institute for Astrophysics and Space Research & Department of Physics,
Massachusetts Institute of Technology, Cambridge, MA 02139-4307, U.S.A.*

burles@mit.edu

ABSTRACT

We present the results of two complementary investigations into the nature of strong (rest equivalent width, $W_r > 1.0 \text{ \AA}$) Mg II absorption systems at high redshift. The first line of questioning examines the complete Sloan Digital Sky Survey Data Release 3 set of quasar spectra to determine the evolution of the incidence of strong Mg II absorption. This search resulted in 7421 confirmed Mg II systems of $W_r > 1.0 \text{ \AA}$ yielding a $> 95\%$ complete statistical sample of 4835 absorbers (systems detected in $S/N > 7$ spectral regions) spanning a redshift range $0.35 < z < 2.3$. The redshift evolution of the comoving line-of-sight number density, $\ell_{\text{Mg}}(X)$ is characterized by a roughly constant value at $z > 0.8$ indicating the product of the number density and gas cross-section of halos hosting strong Mg II is unevolving at these redshifts. In contrast, one observes a decline in $\ell_{\text{Mg}}(X)$ at $z < 0.8$ which we interpret as a decrease in the gas cross-section to strong Mg II absorption and therefore a decline in the physical processes relevant to strong Mg II absorption. Perhaps uncoincidentally, this evolution roughly tracks the global evolution of the star formation rate density. Dividing the systems in W_r sub-samples, the $\ell_{\text{Mg}}(X)$ curves show similar shape with lower normalization at higher W_r values and a more pronounced decrease in $\ell_{\text{Mg}}(X)$ at $z < 0.8$ for larger W_r systems. We also present the results of a search for strong Mg II absorption in a set of 91 high resolution quasar spectra collected on the ESI and HIRES spectrographs. These data allow us to investigate

the kinematics of such systems at $0.8 < z < 2.7$. In this search a total of 22 systems of $W_r > 1.0 \text{ \AA}$ were discovered. These systems are characterized by the presence of numerous components spread over an average velocity width of $\Delta v \approx 200 \text{ km s}^{-1}$. Also, absorption due to more highly ionized species (e.g., Al III, C IV, Si IV) tend to display kinematic profiles similar to the corresponding Mg II and Fe II absorption. We consider all of these results in light of two competing theories previously introduced to explain strong Mg II absorption: post-starburst, supernovae-driven galactic winds and accreting gas in the halos of massive galaxies. The latter model is especially disfavored by the absence of evolution in $\ell_{\text{Mg}}(X)$ at $z > 1$. We argue that the strong Mg II phenomenon primarily arises from feedback processes in relatively low mass galactic halos related to star formation.

Subject headings: quasars: absorption lines (Mg II)

1. Introduction

Starbursting (SB) regions are likely to host rapidly expanding, highly ionized gaseous bubbles (“superwinds”). These bubbles are metal-enriched and powered by the correlated supernovae explosions of the stars on the high end of the SB region’s mass-function. If the starburst is related to a merger event, shock-heating during the interaction may also lead to a wind of ionized gas (Cox et al. 2004). When nested in low enough mass galaxies, these bubbles have a good chance of overpowering their host’s potential well and escaping to pollute the intergalactic medium (IGM) (Furlanetto & Loeb 2003; Madau et al. 2001), though Cox et al. (2004) note that even at high mass merging galaxies may have sufficient energy to produce expanding, gaseous bubbles. At high redshift, such bubbles are expected to travel at velocities of 100 to 1000 km s^{-1} and eventually expand to radii of $\sim 100 \text{ kpc}$. Presumably the winds entrain the metals of prior and recent supernovae activity; therefore, the bubbles may cause metal-line absorption in background sources in the $0.5 < W_r < 5 \text{ \AA}$ range. Indeed, at low redshift the dwarf starbursting galaxy NGC 1569 is observed to possess these characteristics (Martin et al. 2002), as is NGC 1705, another dwarf starburst (Heckman et al. 2001). This enrichment process is believed to have played a leading role in the production of the observed metallicity of the present-day IGM (Madau et al. 2001; Scannapieco et al. 2002), and therefore further observational understanding of this pollution mechanism is key to the refinement of enrichment scenarios. Furthermore, an exploration of the starbursting regions in absorption will constrain dynamic models of starburst winds and serve as an observational bridge for understanding the starbursting process at high redshift.

A link has recently been proposed between these metal-enriched expanding bubbles and the very strong Mg II absorption systems ($W_r > 1.8 \text{ \AA}$) observed in quasar spectra (Bond et al. (2001a), hereafter BCCV). In this paper the cutoff W_r has been relaxed to $> 1.0 \text{ \AA}$, as there is no known specific cutoff to the absorption depth of these systems and, as demonstrated later, smaller systems display features consistent with this phenomena. It is, however, demonstrated that stronger systems are more likely to be associated with this absorption host scenario. Assuming a simple spherical shape for the expanding shell, the expected profile for such a system is two roughly symmetric absorption lobes, corresponding to the cooler, expanding regions of the bubble, one in front and one behind the host galaxy along the line of sight, centered around a kinematically small, hot, non-absorbing region (a spectral "inversion"), where the actual host is located. As the expanding gas is subject to Raleigh-Taylor instability, it is expected to clump, causing distinct kinematic components to appear in the absorption spectra. Cloud-to-cloud metallicity variation may also be expected, a result of unique supernova history and/or incomplete mixing. The expected velocity range of such systems is $\sim 100 - 1000 \text{ km s}^{-1}$. BCCV identified all of these features in the profiles of a small set of strong Mg II absorption systems. Similarly, Steidel et al. (2002) find that gas "infall" from such winds could help explain the kinematics they observed in the spectra of a strong Mg II system. These authors also emphasized that the study of more highly ionized species (e.g. CIV) may further reveal the origin of the Mg II gas and its relation to SN superwinds (see also Bond et al. 2001b).

Based on the assumption that strong Mg II absorbers trace superwinds, and therefore starbursting galaxies, BCCV make a crude prediction of the redshift path density (dN/dz) of Mg II absorption. These authors found it to be consistent with a value extrapolated from the Mg II survey presented in Steidel and Sargent (1992), hereafter SS92, though the comparison suffers from small number statistics. Several goals of the work presented here include an extension of the work of BCCV to higher redshift, to obtain a large statistical sample, and to investigate evolution with redshift.

An interesting correlation could also be made between strong Mg II absorption systems and Lyman Break Galaxies (LBGs), which are thought to frequently harbor starbursting regions. Comparisons of the velocities of the interstellar absorption features with nebular emission lines suggests wind speeds of $200 - 1100 \text{ km s}^{-1}$ (e.g. Pettini et al. 2001). In the gas, one identifies metal-line transitions of both low and high-ion species with significant column densities. Therefore, one may probe the physical characteristics of these winds (e.g. speed, cross-section, ionization state, etc.) through absorption-line studies. In turn, these observations should constrain the incidence and evolution of superwinds during the first $\sim 5 \text{ Gyr}$ of the universe.

A competing scenario for the origin of strong Mg II absorption comes from Mo & Miralda-Escude (1996), hereafter MM96. These authors describe a model where the absorption is associated with gaseous galactic halos in a two-phase structure: a shock heated hot phase and a photoionized phase of clouds moving through the halo. The authors associate this phenomenon with Lyman limit systems, though note that at high redshift ($z > 2$) the model predicts too few Lyman limits. An important aspect of this scenario is that strong Mg II absorption is primarily restricted to the halos of relatively massive galaxies. This is because the shock heated gas can cool only where the gas is dense enough to radiate efficiently, limiting the possible extent of the cold gas. Presumably the authors were motivated by observations showing that strong Mg II systems at $z \lesssim 1$ are frequently identified at impact parameters less than $30 h^{-1}$ kpc from $L \approx L^*$ galaxies (Lanzetta 1993; Steidel 1993). In any case, the MM96 scenario ties Mg II absorption to massive, passively evolving galaxies rather than merging or starburst events.

This paper presents two lines of investigation into the nature of strong (equivalent width¹ $W_r > 1 \text{ \AA}$) Mg II systems: (1) an automated search of the quasar spectra database of the Sloan Digital Sky Survey Data Release 3 (SDSS-DR3) for Mg II systems with $z = 0.35 - 2.3$; and (2) the analysis of a sample of Mg II systems ($z = 0.8 - 2.7$) identified in high resolution spectra of 92 quasars. The paper is organized as follows. § 2 explains the data used in this study and the analysis undertaken on it. § 3 presents our results, including a plot of dN/dz versus redshift, a tabulation of each of the discovered systems, and a plot of interesting metal absorption lines. This section also includes a discussion of the relevance of our results to models of metal pollution of the IGM. The paper concludes in § 4 with a few remarks about future avenues of research.

2. Data and Analysis

This section describes two surveys for strong Mg II lines. In the first, the moderate resolution spectra of Data Release 3 from the Sloan Digital Sky Survey are searched for absorption. This survey provides the largest sample of Mg II systems compiled to date. The second data set is a much smaller sample of high resolution spectroscopy originally obtained to study high z damped Ly α systems. This data extends the search to higher redshift and, more importantly, allows a quantitative assessment of the kinematics of Mg II absorbers.

¹Unless otherwise stated, W_r refers to the equivalent width of the Mg II $\lambda 2796$ transition.

2.1. SDSS-DR3

The first set of data comes from Data Release 3 of the Sloan Digital Sky Survey (SDSS-DR3). The sample has been restricted to SDSS-DR3 quasars with redshift $z_{qso} > 0.35$, for a total of 45023 quasars. SDSS spectroscopy has a resolution $R \approx 2000$ and covers $3800 - 9200 \text{ \AA}$. This coverage implies a redshift search window of $0.35 < z < 2.3$ for the Mg II $\lambda\lambda 2796, 2803$ doublet.

A search and analysis of strong Mg II absorption was carried out in several steps. First each spectrum was continuum fit red-ward of Ly α emission using a Principal Component Analysis to fit the quasar emission lines and a b-spline algorithm to fit the underlying spectrum, which results roughly in a power-law with broad emission features. Second, all 3.5σ features were identified using a Gaussian filter method matched to the spectral resolution of the SDSS data. This method works by convolving a Gaussian with $\sigma = 1$ pixels to both the flux and error arrays. The wavelengths where the convolved flux exceeds the convolved error array by 3.5 are considered significant absorption features and a line list is constructed for each quasar. Each resulting line list was searched for pairs of absorption features with separation matching the Mg II doublet. Finally, the equivalent width of the Mg II 2796 line was measured by directly summing the normalized flux. The equivalent width was measured by summing the difference between the continuum-fitted quasar flux and unity over a redshift centered box of width 3.589 \AA (half the spectral distance between the rest Mg II(2796) and Mg II(2803) lines). This final step is dominated by systematic uncertainty (in particular continuum fitting and contamination due to absorption by both systems at other redshifts and the sky), with an expected typical error of $0.2 - 0.3 \text{ \AA}$. To remove false-positives, a visual confirmation was then made for each system with measured $W_r > 0.8 \text{ \AA}$.

To check the completeness of the survey a Monte-Carlo test was run on a representative sample of quasars. Artificial Mg II systems were added to quasar spectra, which were then searched for absorption as described above. The artificial systems were varied in strength and redshift and the quasars were selected at random from the complete SDSS-DR3 quasar sample. The results of this simulation are displayed in Figure 1. The solid line in the top panel reflect results for $W_r > 1.0 \text{ \AA}$ systems versus redshift. The $W_r > 1.4 \text{ \AA}$ results are displayed with a dashed line. The lower panel displays the W_r of the systems as measured by the search algorithm versus the actual W_r of the added system. The data have been binned and the values displayed are the average detected W_r divided by the actual value, with the errorbars indicating the RMS of the systems in each bin. This figure indicates that this technique of absorption detection is $> 95\%$ complete for $W_r > 1.0 \text{ \AA}$ systems, and provides fairly accurate measurements of W_r , with typical errors of $0.1 - 0.2 \text{ \AA}$. A very small number of outliers in measured W_r were detected in this analysis, primarily a result of sky-

line blending due to small errors in the detected system redshift. This effect was observed in very few systems, and is ignored in the following analysis. There is a slight systematic elevation of measured W_r versus the added W_r , which is an effect of contamination by real absorption systems in a given spectra and is ignored in the following analysis. To further assess the completeness and accuracy of the search algorithm, fifty random quasars were examined by eye. In this sample the automated search missed 2 out of 15 systems, each with $W_r < 0.7 \text{ \AA}$; the W_r measurements of the automated search agreed well with this small sample of found systems. Because of Nyquist biasing, the number of discovered $W_r > 1.0 \text{ \AA}$ systems is expected to be inflated by $W_r < 1.0 \text{ \AA}$ systems included due to error in the measurement of W_r . As the phenomena considered in this work have no specific cut-off in W_r , and as the effect is likely to be small, this error is neglected in the following analysis.

In order to determine the number density of Mg II systems, one must calculate the total redshift path density $g(z)$ of the survey. Large spectral regions, especially at higher redshifts, are highly contaminated by the sky. Simply removing these regions from the analysis would greatly reduce the redshift pathlength available to this study, but it is important to properly account for those regions which are too unreliable to accurately discover Mg II absorption. To account for this issue, the search was limited to regions where the Gaussian fitted ($\sigma = 1 \text{ pix}$) signal-to-noise (of the continuum) $S/N > 7$ per pixel, often resulting in non-contiguous search regions for a given quasar. The analysis of SS92 has been followed with a slight modification. For this work, instead of adding unity to a $g(z)$ redshift bin for each spectrum which contains data for that bin, the decimal percentage of the given bin's redshift range actually covered in each spectra is added. Because strong Mg II systems dampen the noise of a spectra at their wavelength (i.e. Poisson noise is a significant source of error), and the S/N is calculated by dividing the continuum flux by the noise, the S/N at the specific wavelength of a given system will tend to increase over the local average. To protect against over-counting Mg II systems versus $g(z)$, only systems discovered within regions in which the S/N smoothed over a 50 pixel box was greater than 7 are considered for the following analysis. A plot of $g(z)$ for the SDSS search is presented in Figure 2. Limiting the search to smoothed spectral regions of $S/N > 7$ per pixel and a minimum W_r threshold of 0.8 \AA , a total of 6511 Mg II systems were discovered, with 4835 of $W_r > 1.0 \text{ \AA}$, 2594 of $W_r > 1.4 \text{ \AA}$ and 1329 of $W_r > 1.8 \text{ \AA}$. Another 3031 systems were discovered outside of $S/N > 7$ regions, 2586 of which have $W_r > 1.0 \text{ \AA}$.

A histogram of W_r values for the SDSS-DR3 sample is plotted in Figure 3. The distribution is steeply rising at $W_r = 1 \text{ \AA}$, inspiring confidence that the analysis is reasonably complete above this limit. A power-law fit to the $W_r > 1.0 \text{ \AA}$ distribution, $f(W_r) = CW^{-\delta}$, results in the parameters $C = 490.4^{+8.3}_{-9.4}$ and $\delta = 2.24^{+0.04}_{-0.04}$. This fit is plotted as the dashed line in Figure 3. The slope of this function is steeper than that measured in SS92

($\delta = 1.65 \pm 0.03$), but is more consistent with the measurements of others (Tytler et al. 1987, $\delta = 2.2 \pm 0.3$). It is clear from the figure, however, that a power-law is not a good description of the observed distribution, under-predicting the number of systems at low W_r and over-predicting the number of larger systems. The dotted line plotted in the figure represents a fit of a modified Schechter function to the W_r distribution, of the form $f(W_r) = BW_r^{-\phi} e^{-W_r}$, which is a much better fit to the data, particularly at high W_r . The best fit values for this functional form are $B = 2398^{+72}_{-71}$ and $\phi = 1.19 \pm 0.07$. It is likely that allowing the characteristic W_r , W_r^* , to be a fitted variable rather than setting it to unity would improve the fit even further. Because this value has no bearing on the following discussion, this fitting and its interpretation are left to future work. All the fits were performed using unbinned, Maximum Likelihood analysis. The errors are 95% confidence limits.

Table 1 presents the SDSS quasar name, RA and DEC, emission redshift, the Mg II redshift, and W_r of each $W_r > 1.0 \text{ \AA}$ Mg II system discovered in the automated SDSS search, including those which passed the 'by-eye' confirmation but were eliminated from further analysis by the $S/N > 7$ per pixel criterion.

2.2. High Resolution Observations

The second set of quasar spectra used in this study includes 51 high S/N spectra ($FWHM \sim 6.3 - 8.4 \text{ km s}^{-1}$) taken with the High Resolution Echelle Spectrometer (HIRES; Vogt et al. 1994) on the Keck I 10m telescope. These data were recorded and reduced as part of the UCSD/Keck I Damped Ly α Abundance Database and a full discussion of the reduction process can be found in Prochaska et al. (2001). The high resolution sample also includes 41 $R \sim 8000$ spectra taken on the ESI spectrograph on Keck II. These data were collected as a part of the ESI/KECK II Damped Ly α Abundance Database, details of which can be found in Prochaska et al. (2003). Table 2 summarizes the spectra searched in this study, presenting the name of each quasar, z_{em} , data collection instrument (with 1 and 2 referring to HIRES and ESI, respectively), the lower and upper limits of redshift available for Mg II detection, and information on discovered absorption systems. It should be noted that every spectrum in this data set contains a damped Ly α system; these were ignored throughout the Mg II analysis.

For each spectrum a 'by-eye' search was made for Mg II absorption systems. Given the strength of this doublet, these systems are conspicuous. After identifying a Mg II system, its redshift, equivalent width (Mg II 2796) and velocity width were measured, and the spectrum was searched for absorption due to other transitions associated with the system. The velocity width (Δv) calculation followed the analysis of Prochaska and Wolfe (1997), i.e., the region

bounding 90% of the total optical depth in an unsaturated transition (typically Fe II 2600). The kinematic complexity of each system was also assessed, generally using complementary, non-saturated metal absorption lines (e.g. Fe II 2600). This measure is a simple summation of the distinct velocity components visible and was made due to the importance of absorption complexity to the arguments of BCCV. Because the ESI spectra are of lower resolution than those taken with HIRES, the observed complexity is expected to be reduced. Velocity structure will be lost for components separated by less than 45 km s^{-1} , especially in saturated absorption features. On the other hand, the spectra are sensitive to structure in the velocity profiles for components separated by greater than $\approx 50 \text{ km s}^{-1}$.

The redshift path density $g(z)$ has been calculated in a similar manner as the SDSS sightlines. The only significant difference is that spectral gaps inherent to the HIRES instrument add some uncertainty to this calculation. A possible prescription for accounting for the HIRES spectral gaps involves disqualifying those spectral areas immediately preceding and following the gaps, as only one half of the doublet is not enough to determine its nature. Because the systems of interest in this work are quite strong and because the wavelength coverage allows for investigation and confirmation of systems based on other metal absorption lines (e.g. Fe II), this prescription was not followed and only the HIRES spectral gaps large enough to hide both components of a Mg II absorption doublet were disqualified in the calculation of $g(z)$. Figure 4 presents $g(z)$ for the high resolution sample. Clearly this high-resolution data extends to a higher redshift than available in the SDSS sample, though the small number of sightlines limits the significance of statistical results gleaned from this data.

The high resolution survey is complete to below the $W_r = 1.0 \text{ \AA}$ level. Both the ESI and HIRES datasets provide more than enough resolution and S/N for confidence in this statement. More than 50 Mg II systems with $W_r < 1 \text{ \AA}$ were discovered in the search, though disregarded for the work presented here. At very long wavelengths ($\sim 10000 \text{ \AA}$ in the ESI spectra), sky lines can confuse the search for Mg II systems. In a few particularly bad cases data are disqualified for this analysis, though the majority of spectra remained clear enough to easily identify absorption systems of the strength considered in this work. An example is presented in Figure 5: a plot of the Mg II system with $W_r = 0.56 \text{ \AA}$ located at $z = 2.51$ ($\sim 9800 \text{ \AA}$) in the spectrum of Q1337+11. Even crowded by the sky, this system is easily identified though it is only half as strong as the systems of interest to this study.

The 22 $W_r > 1.0 \text{ \AA}$ Mg II absorption systems discovered in this survey are depicted in Figure 6. For each system the Mg II 2796 absorption line is displayed in relative velocity (km s^{-1}) space with 0 km s^{-1} centered on the redshift reported in Table 2. When more than one system was discovered in a given quasar spectrum, the lower and higher redshift systems

are labeled with a (1) and (2), respectively (no more than two systems were detected in any one spectrum). An unsaturated or mildly saturated transition (usually an Fe II line) is also displayed for each system.

Six ($\sim 50\%$) of the systems for which spectra at the relevant wavelength were available (both observed in the quasar spectrum and not lost to the Ly α forest) contained evidence of absorption due to Si IV, C IV, and Al III. These lines are displayed in Figure 7, where the systems are labeled as in Figure 6. These lines are displayed in relative velocity space with 0 km s^{-1} centered at the system redshift found in Table 2.

3. The Incidence of Strong Mg II Absorption

3.1. Observations of and Fits to $\ell_{\text{Mg}}(X)$

One means of investigating the physical nature of strong Mg II systems is to examine their incidence as a function of cosmological time. The most convenient and least ambiguous measure of this incidence is $\ell_{\text{Mg}}(X)$, the line-density of absorbers per comoving Mpc. The incidence of a given class of absorbers at any redshift is proportional to their covering fraction on the sky. If the Mg II systems are a non-evolving population (i.e. constant number per comoving Mpc^{-3} n_0 and constant cross-section σ_0), then one would predict $\ell_{\text{Mg}}(X) = n_0\sigma_0$. Should the number density or cross-section evolve with redshift, then n_0 and σ_0 are replaced with $n(z)$ and $\sigma(z)$. If, for example, strong Mg II systems are related to merger events, then one would expect $n(z)$ to track the merger rate, predicted to be proportional to $(1+z)^3$ (e.g., Patton et al. 1997), which implies a steep redshift dependence for $\ell_{\text{Mg}}(X)$. Furthermore, because the number density evolution of halos in hierarchical cosmology is a sensitive function of mass, making comparisons with the evolution of $\ell_{\text{Mg}}(X)$ may indicate the mass of the systems giving rise to Mg II absorption.

Historically, analysis has focused on the incidence of Mg II systems as a function of redshift, $\ell_{\text{Mg}}(z)$ (frequently written as dN/dz). Interpretation of this measure is somewhat ambiguous, because the evolution is influenced by the expansion of the universe as well as any evolution of the absorbers in question

$$\ell_{\text{Mg}}(z) = \ell_{\text{Mg}}(X) * (c/H_0)(1+z)^2[\Omega_M(1+z)^3 + \Omega_\Lambda]^{-1/2}. \quad (1)$$

For this reason the majority of the analysis below is presented in terms of $\ell_{\text{Mg}}(X)$, which renders more obvious the trends discussed. For comparison to previous work, statistics of $\ell_{\text{Mg}}(z)$ are also presented.

Figure 8 presents $\ell_{\text{Mg}}(X)$ for the Mg II systems identified in the SDSS-DR3 sample over the redshift range $z = 0.35 - 2.3$. The vertical errorbars assume Gaussian statistics while the horizontal errorbars indicate the size of each redshift bin. The SDSS results are displayed in three sets: the closed triangles represent the entire $W_r > 1.0 \text{ \AA}$ dataset, the open squares indicate systems of $1.0 \text{ \AA} < W_r < 1.4 \text{ \AA}$, and the cross-hatches represent $W_r > 1.8 \text{ \AA}$. The data plotted in this figure are also listed in Table 3, as are the results for several other samples in W_r . Qualitatively, the samples shown in Figure 8 exhibit similar $\ell_{\text{Mg}}(X)$ evolution. At redshifts $z > 0.8$, $\ell_{\text{Mg}}(X)$ is nearly constant and linear fits yield slopes consistent with zero at the 95% c.l. At $z < 0.8$, in contrast, each sample exhibits a decrease in $\ell_{\text{Mg}}(X)$. For the $1.0 \text{ \AA} < W_r < 1.4 \text{ \AA}$ sample the decline is marginally significant ($\sim 1\sigma$), while the effect is highly significant for any sample with $W_r > 1.4 \text{ \AA}$.

We have considered two functional forms to describe the evolution of $\ell_{\text{Mg}}(X)$ with redshift: (1) a linear fit $\ell_{\text{Mg}}(X) = b + mz$ and (2) an exponential fit $\ell_{\text{Mg}}(X) = N \exp(-z_0/z)$. Fitting a line to the $1.0 \text{ \AA} < W_r < 1.4 \text{ \AA}$ sample yields a slope consistent with zero: $m = 0.002 \pm 0.003$. In contrast, the strongest Mg II absorbers ($W_r > 1.8 \text{ \AA}$) have $m = 0.011 \pm 0.002$. Therefore, there is steeper increase in $\ell_{\text{Mg}}(X)$ for the larger W_r absorbers, with the majority of the difference occurring at $z < 1$. These functional forms have very large reduced χ^2 values, however, and are not good descriptions of the data. The exponential fits, in contrast, are a reasonable model of the data as these allow for a sharp dropoff of incidence at low redshift. Using standard maximum likelihood methods, we find $N = 0.044 \pm 0.003$ and $z_0 = 0.12 \pm 0.07$ for the $1.0 \text{ \AA} < W_r < 1.4 \text{ \AA}$ systems, $N = 0.037 \pm 0.003$ and $z_0 = 0.47 \pm 0.10$ for the $W_r > 1.8 \text{ \AA}$ systems, and $N = 0.11 \pm 0.006$ and $z_0 = 0.28 \pm 0.05$ for the full $W_r > 1.0 \text{ \AA}$ dataset. These results are summarized in Table 4.

For comparison to previous work, power-law fits to the $\ell_{\text{Mg}}(z)$ values of the form $N_0(1+z)^{\gamma_0}$ have also been performed. We stress, however, that such fits are no longer a good description of the data. In particular, this functional form cannot describe both the increase in $\ell_{\text{Mg}}(X)$ at low redshift and the roughly constant value at $z = 1$ to 2. Nevertheless, this analysis was done for several cuts of the data. The maximum likelihood values for N_0 and γ_0 are $N_0 = 0.084$, $\gamma_0 = 1.40$ for $W_r > 1.0 \text{ \AA}$, $N_0 = 0.051$, $\gamma_0 = 0.99$ for $1.0 \text{ \AA} < W_r < 1.4 \text{ \AA}$, and $N_0 = 0.016$, $\gamma_0 = 1.92$ for $W_r > 1.8 \text{ \AA}$. Table 4 reports central values for N_0 and γ_0 , as well as 95% confidence limits for each of the three fits. It should be noted that the values of γ_0 and N_0 are highly correlated. Previous work on Mg II absorption has yielded similar, if somewhat steeper, results. SS92 find that for $W_r > 1.0 \text{ \AA}$ systems, $dN/dz \propto (1+z)^{2.24 \pm 0.76}$. Also consistent with the results of SS92 is the increase in γ_0 with minimum equivalent width. We emphasize, however, that the differences in γ_0 are dominated by the evolution in $\ell_{\text{Mg}}(X)$ at low redshift because all of the sub-samples have nearly constant $\ell_{\text{Mg}}(X)$ at $z > 1$. Altogether, the $W_r > 1.0 \text{ \AA}$ sample has an average incidence per unit redshift $\ell_{\text{Mg}}(z) = 0.174 \pm 0.002$.

for the redshift region $0.35 \leq z \leq 2.3$. This value is consistent with but 25% lower than the value reported by SS92 for the redshift range $0.2 \leq z \leq 2.2$ and are well matched to those of Nestor et al. (2004), who report results from the SDSS Early Data Release.

3.2. Selection Bias

It is important to understand and constrain possible biases in the SDSS-DR3 quasar sample. The value of $\ell_{\text{Mg}}(X)$ is sensitive to observational bias in several forms. For example, if the Mg II systems are themselves massive enough to gravitationally lens, and thus brighten, their background quasars then the SDSS-DR3 would be statistically biased toward observing quasars which exhibit strong Mg II absorption (Menard 2005). This would lead to an underestimation of $g(z)$ and an overestimation of $\ell_{\text{Mg}}(X)$. The opposite effect may result if quasar spectra are reddened by dust in the Mg II host systems. Indeed, this bias is of particular concern, as many of the systems in this sample will be associated with damped Ly α systems (Nestor et al. 2003) and such systems may cause reddening in the spectra of background quasars (Pei et al. 1991; Murphy & Liske 2004).

Following the analysis of Murphy & Liske (2004) to address the matter of gravitational lensing, two averaged bootstrap samples of quasars free of strong Mg II absorption were created. The first of these samples was free of Mg II absorption in the range of $1.0 \text{ \AA} < W_r < 1.4 \text{ \AA}$, the second of $W_r > 1.8 \text{ \AA}$ systems. These quasars were chosen to reproduce the redshift distribution of those sets of Mg II absorption-hosting quasars, but were otherwise chosen at random. Repeating this process many times uncovered the average non-absorption quasar magnitude distribution, which was then compared to the magnitude distribution of those quasars with Mg II absorption. This analysis revealed no signal of gravitational lensing in either the $1.0 \text{ \AA} < W_r < 1.4 \text{ \AA}$ or the $W_r > 1.8 \text{ \AA}$ datasets. Indeed, two-sided Kolmogorov-Smirnov tests reveal no evidence of differing magnitude distributions between the absorption and non-absorption datasets in either W_r bin, with KS probabilities ranging from 0.2 – 0.6.

Dust however, does seem to affect the spectra on average of those quasars hosting the strongest of the Mg II absorption systems. By building samples of quasars similar to the controls used in the lensing test (but now also constraining magnitude distributions of the control samples), composite ‘non-absorption’ quasar spectra were compiled, red-ward of Ly α emission and in the rest wavelength of the quasar emission, for the two sets of W_r Mg II systems described above. The second and fourth panels of Figure 9 display these spectra, as well as composite ‘absorption’ spectra, for the two Mg II absorption W_r bins. Also plotted are power-law fits to these spectra, $f(\lambda) \propto \lambda^\alpha$. Dust will preferentially absorb bluer light, tilting the spectrum and lowering the absolute value of α .

The first and third panels represent the result of dividing the composite Mg II spectra with the control spectra. The power-law fits to the $1.0 \text{ \AA} < W_r < 1.4 \text{ \AA}$ composite spectrum and its companion control spectrum are nearly identical, $|\Delta(\alpha)| \sim 0.02$. These systems, therefore, are unlikely to impose an important dust bias. The larger W_r sample clearly displays a dust signature, as seen in the divided spectrum in the upmost panel of Figure 9. For this sample $|\Delta(\alpha)| \sim 0.11$. Assuming Small Magellanic Cloud type extinction and employing the fitting formula of Pei (1992), this $|\Delta(\alpha)|$ corresponds to a color excess $E(B - V) \sim 0.01$. This is an important result, especially as there are known quasar selection effects within SDSS, which uses colors in addition to apparent magnitude to select quasars for spectroscopic follow-up (Richards et al. 2002). Given the small color excess implied by the measured $|\Delta(\alpha)|$, however, these effects are likely to be small. A full consideration of these effects will be the subject of a future paper. For now, we note that the effect of reddening would generally be to under-measure $\ell_{\text{Mg}}(X)$. The net effect could be a systematic shallowing of $\ell_{\text{Mg}}(X)$ especially at $z > 1$, although the reddening is sufficiently small that the corrections to $\ell_{\text{Mg}}(X)$ should be minor.

3.3. Implications and Interpretations

The evolution of $\ell_{\text{Mg}}(X)$ described by Figure 8 has several implications for the physical processes relevant to Mg II systems. First, the near constancy of $\ell_{\text{Mg}}(X)$ over the $\approx 3 \text{ Gyr}$ spanning $z = 2$ to 0.8 indicates the cross-section to strong Mg II systems is very likely to be dominated by dark matter halos with masses $M \ll 10^{12} M_\odot$. Although structure forms much earlier in the ΛCDM cosmology than an Einstein de Sitter model, the number density of galaxies with $M > M_*(z = 2) \approx 10^{11} M_\odot$ increases exponentially over this epoch (e.g. Jenkins et al. 2001). If these massive galaxies dominated the cross-section, then σ would have to decrease exponentially to yield constant $\ell_{\text{Mg}}(X)$. We consider such a coincidence to be highly unlikely. It is far more reasonable to physically associate the phenomenon with galaxies having mass $M < M_*(z = 2)$ and assume a nearly constant cross-section during this epoch. Second, the decline in $\ell_{\text{Mg}}(X)$ at $z < 0.8$ indicates the cross-section to strong Mg II systems is decreasing in time. This conclusion applies particularly to the $W_r > 1.8 \text{ \AA}$ absorbers where the decrease in $\ell_{\text{Mg}}(X)$ is secure. For the same argument as above, the number density of dark matter halos is either constant (for $M \ll M_*$) or increasing substantially (for $M \gg M_*$). A decrease in $\ell_{\text{Mg}}(X)$ therefore, can only be explained by a decrease in σ . The observations imply the processes responsible for strong Mg II absorbers are ‘turning off’ at $z \sim 1$. Third, one identifies a rough correspondence between the star formation history of the universe (Madau et al. 1996) and $\ell_{\text{Mg}}(X)$. Granted the two quantities track one another over the redshift range $z = 0.5$ to 2 , it is tempting to connect the strong Mg II systems with processes

related to active star formation (e.g. galactic winds, starbursts).

We now examine the implications of the evolution of $\ell_{\text{Mg}}(X)$ in terms of the two models described in the introduction: (1) a starburst scenario where the incidence and kinematics of strong Mg II systems are determined by feedback processes (BCVS); and (2) infalling gas in the outer halos of massive galaxies (MM96). An important prediction of the MM96 scenario is that $\ell_{\text{Mg}}(X)$ should steeply decline at high redshift once the characteristic dark matter halo mass M_* becomes smaller than the typical halo mass giving rise to strong Mg II absorption. In the MM96 scenario, the halo mass is $\sim 10^{12}M_\odot$, which is necessary to insure the halo has a significant reservoir of cool, photoionized gas (MM96). Within the Λ CDM cosmology with $\sigma_8 = 0.9$, $M_* = 10^{12}M_\odot$ at $z = 0.75$. Therefore, this model predicts a steep decline in $\ell_{\text{Mg}}(X)$ at $z > 1$ which is not observed. As noted above, to adopt a model where strong Mg II absorption arises in an unevolving population of dark matter halos, the typical mass would need to be less than $M_*(z = 2) \approx 10^{10.5}M_\odot$. Therefore, we conclude that the majority of strong Mg II absorbers do not arise in massive halos typical of the $W_r \approx 0.3\text{\AA}$ population at $z \sim 1$. In fairness, we note that the MM96 model was primarily introduced to explain the $W_r \approx 0.3\text{\AA}$ Mg II systems which may have a different origin than the strong Mg II absorbers considered in this paper.

It is more difficult to compare the observations against the starburst scenario because there does not exist a well-developed model. Nevertheless, consider the following arguments. At $z \sim 1$, the dark matter halo merger rate is expected to scale as $(1+z)^3$ (Patton et al. 1997). If one assumes the starburst phenomenon is merger-driven, then the simple prediction is an increase in $\ell_{\text{Mg}}(X)$ with increasing redshift. Indeed, this is observed from $z = 0.3$ to 0.8 , yet all of the sub-samples are inconsistent with even a $(1+z)$ increase in $\ell_{\text{Mg}}(X)$ at $z > 1$. Because the incidence is the product of the number density and cross-section of the halos, one could envision a scenario where σ is decreasing with redshift as n increases such that $\ell_{\text{Mg}}(X)$ remains roughly constant. For example, the Mg abundance could be much lower at higher redshift or the velocity fields more quiescent, but these explanations are rather unlikely for a starburst model. Recent observational results of Len et al. (2004) suggest another possible solution. These authors find that the galaxy merger rate evolves much more shallowly with redshift than dark matter haloes, $(1+z)^{0.51 \pm 0.28}$, a much better match to the Mg II observations.

As noted above, the general trend of $\ell_{\text{Mg}}(X)$ roughly tracks the global density of star formation. That is, the star formation rate (SFR) density is described as roughly constant from $z = 1$ to 2 (where it is not well constrained) and decreases by a factor of several from $z = 1$ to today. Although the correspondence between the incidence of strong Mg II absorbers and the SFR density could be simple coincidence, it may be expected if the absorption

systems arise from feedback processes related to star formation. The correspondence may suggest that significant star formation is required to maintain a large cross-section to strong Mg II absorption, i.e. this phase is short-lived in galactic halos and requires continued input to maintain the observed incidence at $z = 1$ to 2. At the very least, we consider the similarity to be at least anecdotal evidence in favor of a starburst scenario.

The actual value of the incidence of strong Mg II absorption – as opposed to its evolution – provides an important constraint on the hypotheses of massive galactic halos and starbursts. The phenomenology of MM96 implies a typical impact parameter for Mg II absorption of $\rho \sim 30 \text{ h}^{-1} \text{ kpc}$. Using $\ell_{\text{Mg}}(X) \sim 3 \times 10^{-5} h \text{ Mpc}^{-1}$ at $z \sim 1$, the value measured in this work for $W_r > 1.0 \text{ \AA}$ systems, a number density $n \sim 0.01 h^3 \text{ Mpc}^{-3}$ is measured for large, quiescent galaxies at this redshift. It should be recalled that the measured $\ell_{\text{Mg}}(X)$ for Mg II at this redshift may be somewhat influenced by merging systems, so the value used for $\ell_{\text{Mg}}(X)$ in this calculation should be considered an upper-limit. Again assuming standard concordance cosmology and using the mass function introduced by Jenkins et al. (2001), the mass of halos with $n \sim 0.01 - 0.03 h^3 \text{ Mpc}^{-3}$ is $M \sim 10^{11} M_{\odot}$. Similar to our previous conclusions, we find that the MM96 scenario is nonviable at $z > 1$ if one adopts their typical mass halo of $10^{12} M_{\odot}$ unless one extends the impact parameter to an unlikely $\rho \sim 100 \text{ kpc}$.

Turning to the starburst hypothesis of BCCV, the observations can be used with previous work on superwinds and LBGs to constrain the required impact parameter of the outflows. If high redshift MgII systems do correspond to SB galaxies, one expects them to trace LBGs, also thought to harbor starbursts. Using the measured number density $n \sim 0.016 h^3 \text{ Mpc}^{-3}$ for LBGs at $z \sim 3$ (Steidel et al. 1999), and assuming the value of $\ell_{\text{Mg}}(X)$ observed at $z = 2$ for the $W_r > 1 \text{ \AA}$ sample ($2 \times 10^{-5} h \text{ Mpc}^{-1}$), the predicted σ for merging MgII systems at $z = 3$ is $\sigma \sim 10^{-3} h^{-2} \text{ Mpc}^2$. The value of $\ell_{\text{Mg}}(X)$ used in this calculation may be considered a maximum, as the overall sample of Mg II systems discovered in this survey is likely to be polluted with large-scale processes, Damped Ly α absorption systems, or other systems, and thus the resultant value of σ is also a maximum. To determine whether this value is consistent with the wind hypothesis, theoretical upper and lower bounds on σ may be used. Assuming a $v_{\text{bubble}} \sim 100 \text{ km s}^{-1}$ and a bubble age $t_r \sim 60 \text{ Myr}$ (BCCV, a lower limit equal to the expected time-scale of the SB), the approximate impact parameter will be $\sigma \sim 1 \times 10^{-4} \text{ Mpc}^2$. The expansion time and velocity used for this calculation are both lower limits, so this is a lower limit. Computer simulations presented in Furlanetto & Loeb (2003) find the maximum size of these bubbles (after very long evolutionary periods) to correspond to $\sigma \sim 3 \times 10^{-2} \text{ Mpc}^2$. The gas in such large bubbles, however, may be of too low density to give rise to strong MgII absorption, so this should be considered an extreme upper limit. In any case, the cross-section determined from MgII absorption and LBG data is consistent with the theory that superwinds are the primary hosts of high redshift MgII

absorption.

4. Kinematics

Examining the profiles in Figure 6, it is evident that the majority demonstrate at least one of the three criteria discussed in BCCV for the identification of superwind driven galactic bubbles. Because these features were clearly present in even the weaker W_r systems, the BCCV criterion of $W_r > 1.8 \text{ \AA}$ has been relaxed to $W_r > 1.0 \text{ \AA}$. Based primarily on unsaturated transitions (usually a Fe II line), the majority ($\sim 80\%$) of the discovered systems exhibit some degree of complexity, though as discussed above, kinematic features of width $\Delta v \leq 45 \text{ km s}^{-1}$ are unobservable in the ESI spectra. Because every system discovered in a HIRES spectrum displays a great deal of spectral complexity, and as many of these features are kinematically closer than the above specified limit, it is probably a safe assumption that most or all of the systems studied in this work conform to the complexity criterion introduced out by BCCV.

Figure 10 presents a histogram of the velocity widths of the high resolution sample. Clear is the cutoff at $\sim 100 \text{ km s}^{-1}$ which corresponds to the $W_r > 1.0 \text{ \AA}$ imposed on this study (although recall that the Δv measurements are based on unsaturated profiles). The velocities range from $\Delta v = 66 \text{ km s}^{-1}$ for the $z = 1.328$ system toward Q1331+17 to $\Delta v = 470 \text{ km s}^{-1}$ for the $z = 1.339$ system toward PSS2241+1352, with the majority of systems having $\Delta v \sim 200 \text{ km s}^{-1}$. In the idealized case of a spherical shell expanding with constant velocity v_{shell} , the velocity width for an impact parameter of $R/2$ is $\sqrt{3}v_{shell}$. Therefore, the median velocity width for this sample corresponds to a shell speed of $v_{shell} \sim 150 \text{ km s}^{-1}$. This value is consistent, though on the low end, with numbers observed for local galactic superwinds (Heckman et al. 2000) and those predicted from numerical simulations (e.g., Strickland & Stevens 2000). An important and somewhat unexpected result of this analysis is that very few Mg II systems show $\Delta v > 250 \text{ km s}^{-1}$. If this gas is tracing winds arising from starburst systems, it is evident that the optical depth of rapidly expanding ‘bubbles’ at $z \sim 1.5$ is small: $\tau < 1.0 \times 10^{-5} h \text{ Mpc}^{-1}$ (95% c.l.).

In one respect, the data displayed in Figure 7 are generally unsupportive of the Mg II absorber-superwind hypothesis. In a wind model, one envisions a cold, expanding shell of gas which envelopes a rarefied, hot region which in turn surrounds the post-SB galaxy. In this scenario, one would not expect to observe high-ionization state particles (e.g. Si IV) in the same distribution as the colder gas (Mg II; Strickland & Stevens (2000)). One might expect the higher-ionization state gas to be distributed in a kinematically narrower region (it is no longer expanding). Alternatively, the gas may exhibit turbulent velocities

at the virial velocity dispersion of the galaxy and not conform to the clump patterns of the gas in the shell. In either case, these trends are not observed in those systems with high-ionization lines. Figure 7 shows a clear trend for high- and low-ionization state gas to share the same regions of km s^{-1} space and to often display similar clumping patterns. This result is consistent with the work of Churchill et al. (1999), who reported strong kinematic links between Mg II and C IV absorption in the redshift range $0.4 \leq z \leq 1.4$, and discussed consequences for both the above scenario and that proposed by MM96, which involves cold bubbles of gas confined by pressure in a hot gas medium.

The construction of MM96 also implies different kinematic situations for the hot and cold gas, a prediction not supported by the data. Indeed, the models presented in MM96 predict that systems showing strong Mg II absorption (large galaxies) should contain little if any C IV absorption, which is clearly ruled out by the data. A suggestion put forward to fix this discrepancy is a “warm” phase of collisionally ionized gas in an interface between the cold bubbles and the hot medium. This would explain the observed kinematic link between Mg II and more highly ionized species (in either the expanding bubble or two-phase gaseous halo scenarios), though the authors point out that the amount of collisionally ionized C IV found in such a phase would likely be small. There is also the possibility that C IV arises at higher radii than the simple models of MM96 consider. This solution, while providing for more C IV absorption, does not provide a simple explanation for the observed kinematic link between species. More sophisticated models of the two-phase halo structure are needed to clarify this issue.

5. Concluding Remarks

There are many open questions left in the task of assigning a particular phenomenology to strong Mg II absorption. Detailed simulations of superwinds would be useful in pinning down the expected absorption profile of such a system, as well as providing information on expected metallicities and temperatures. A handful of strong Mg II absorption-selected galaxies have been studied kinematically (see Steidel et al. 2002; Churchill et al. 2000), with varying results, though the number remains small and little consideration has gone into the link stipulated in this work. A more comprehensive survey over a larger redshift range would allow for stronger statements regarding the correlation between these absorbers and galaxy populations, as well as a refined understanding of their kinematic nature. Optical studies could only provide results at low redshift, but confirmation of the SB and post-SB nature expected of the hosting galaxies, even for low- z examples, would strengthen the argument considerably. Adaptive optics might be useful here, and a program has been begun

at Lick Observatory to obtain AO images of a few quasars known to harbor low redshift, strong Mg II systems in an attempt to morphologically identify these systems. We are also performing a separate imaging program with ACS on the Hubble Space Telescope (Cycle 14) to cover a wider range of redshift. Finally, with the advent of infrared spectrographs (e.g. the GNIRS instrument on Gemini South) and the availability of large numbers of bright, high redshift quasars (as in the SDSS DR3), the phenomenon can be studied to very high redshift ($z \sim 4$). In particular, it is critical to further test the assertion that strong Mg II systems trace processes related to star formation.

The authors wish to recognize and acknowledge the very significant cultural role and reverence that the summit of Mauna Kea has always had within the indigenous Hawaiian community. We are most fortunate to have the opportunity to conduct observations from this mountain. We also acknowledge the Keck support staff for their efforts in performing these observations. We acknowledge the tremendous effort put forth by the SDSS team to produce and release the SDSS survey. We thank M. Kuhlen, J. Primack, and T.J. Cox for helpful discussions. Finally, we would like to thank the anonymous referee of this paper who generated a number of useful comments and suggestions. GEP and JXP are supported by NSF grant AST-0307408.

REFERENCES

- Adelberger, K. L., Steidel, C. C., Shapley, A. E., & Pettini, M. 2003, *ApJ*, 584, 45
- Bolton, A. S., Burles, S., Schlegel, D. J., Eisenstein, D. J., & Brinkmann, J. 2004, *AJ*, 127, 1860
- Bond, N. A., Churchill, C. W., Charlton, J. C., & Vogt, S. S. 2001, *ApJ*, 562, 641
- Bond, N. A., Churchill, C. W., Charlton, J. C., & Vogt, S. S. 2001, *ApJ*, 557, 761
- Chen, H. W., Marzke, R. O., McCarthy, P. J., Martini, P., Carlberg, R. G., Persson, S. E., Bunker, A., Bridge, C. R., & Abraham, R. G. 2003, *ApJ*, 586, 745
- Churchill, C. W., Kacprzak, G. G., Steidel, C. C. AAS Meeting 205, 129.04
- Churchill, C. W., Mellon, R. R., Charlton, J. C., Jannuzi, B. T., Kirhakos, S., Steidel, C. C., & Schneider, D. P. 2000, *ApJ*, 543, 577
- Churchill, C. W., Mellon, R. R., Charlton, J. C., Jannuzi, B. T., Kirhakos, S., Steidel, C. C., & Schneider, D. P. 1999, *ApJ*, 519, L43

- Cox, T. J., Primack, J., Jonsson, P., & Somerville, R. 2004, preprint (astro-ph:0402675)
- Furlanetto, S. R. & Loeb, A. 2003, ApJ, 588, 18
- Heckman, T. M., Lehnert, M. D., Strickland, D. K., & Armus, L. 2000, ApJS, 129, 493
- Heckman, T. M., Sembach, K. R., Meurer, G. R., Strickland, D. K., Martin, C. L., Calzetti, D., Leitherer, C. 2001, /apj, 554, 1021
- Holmberg, E. 1975, in *Stars and Stellar Systems, 9, Galaxies and the Universe*, ed(s)., A. Sandage, M. Sandage, & J. Kristian, (Chicago: Univ. Chicago Press), p. 123
- Jenkins, A., Frenk, C. S., White, D. M., Colberg, J. M., Cole, S., Evrard, A. E., Couchman, H. M. P., & Yoshida, N. 2001, MNRAS, 321, 372
- Lanzetta, K. M., Wolfe, A. M., & Turnshek 1987, ApJ, 322, 739
- Lanzetta, K.M. 1993, in *The Environment and Evolution of Galaxies*, ed. J.M. Shull & H.A. Thronson, Jr. (Boston: Kluwer Academic Publishers), p. 237
- Lanzetta, K. M., Yahata, N., Pascarelle, S., Chen, H. W., Fernandez-Soto, A. 2002, ApJ, 570, 492
- Lin, L., Koo, D. C., Willmer, C. N. A., Patton, D. R., Conselice, C. J., Yan, R., Coil, A. L., Cooper, M. C., Davis, M., Faber, S. M., Gerke, B. F., Guhathakurta, P., Newman, J. A. 2004, ApJ, 617, L9
- Madau, P., Ferguson, H.C., Dickinson, M.E., Giavalisco, M., Steidel, C.C., & Fruchter, A. 1996, MNRAS, 283, 1388
- Madau, P., Ferrara, A., & Rees, M. J. 2001, ApJ, 555, 92
- Martin, C. L., Kobulnicky, H. A., & Heckman, T. M. 2002, ApJ, 574, 663
- Menard, B. 2005, ApJ, 630, 28
- Misawa, T., Tytler, D., Iye, M., Storrie-Lombardi, L. J., Suzuki, N., & Wolfe, A. M. 2002, AJ, 123, 1847
- Mo, H. J. & Miralda-Escude, J. 1996, ApJ, 469, 589
- Murphy, M. T., Liske, J. 2004, MNRAS, 354, 31
- Nestor, D. B., Rao, S., M., Turnshek, D. A., & Vanden Berk, D. 2003, /apj, 595, 5

- Nestor, D. B., Turnshek, D. A., & Rao, S. M. 2004, astro-ph/0410493
- Patton, D. R., Pritchet, C. J., Yee, H. K., Ellingson, E., & Carlberg, R. G. 1997, ApJ, 475, 29
- Pei, Y. C., Fall, S. M., Bechtold, J. 1991, ApJ, 378, 6
- Pei, Y. C. 1992, ApJ, 395, 130
- Pettini, M., Kellogg, M., Steidel, C. C., Dickenson, M., Adelberger, K. L., & Giavalisco, M. 1998, ApJ, 508, 539
- Pettini, M., Shapley, A. E., Steidel, C. C., Cuby, J-G., Dickinson, M., Moorwood, A. F. M., Adelberger, K. L., Giavalisco, M. 2001, ApJ, 554, 981
- Pettini, M., Madau, P., Bolte, M., Prochaska, J.X., Ellison, S.L., & Fan, X. 2003, ApJ, 594, 695
- Prochaska, J. X., & Wolfe, M. W. 1997, ApJ, 487, 73
- Prochaska, J. X., Wolfe, A. M., Tytler, D., Burles, S., Cooke, J., Gawiser, E., Kirkman, D., O’Meara, J. M., & Storrie-Lombardi, L. 2001, ApJS, 137, 21
- Prochaska, J.X., Gawiser, E., Wolfe, A.M., Cooke, J., & Gelino, D. 2003, ApJS, 147, 227
- Richards, G.T. et al. 2002, AJ, 123, 2945
- Scannapieco, E., Ferrara, A., & Madau, P. 2002, ApJ, 574, 590
- Schaye, J. 2001, ApJ, 559, L1
- Schaye, J., Aguirre, A., Kim, T.-S., Theuns, T., Rauch, M., & Sargent, W.L.W. 2003, ApJ, 596, 768
- Spergel, D. N., Verde, L., Peiris, H. V., Komatsu, E., Nolte, M. R., Bennett, C. L., Halpern, M., Hinshaw, G., Jarosik, N., Kogut, A., Limon, M., Meyer, S. S., Page, L., Tucker, G. S., Weiland, J. L., Wollack, E., Wright, E. L. 2003, ApJS, 148, 175
- Steidel, C. C., & Sargent, W. L. W. 1992, ApJS, 80, 1
- Steidel, C.C. 1993, *The Environment and Evolution of Galaxies*, ed. J.M. Shull & H.A. Thronson, Jr., (Boston: Kluwer Academic Publishers), p. 263
- Steidel, C. C., Adelberger, K. L., Giavalisco, M., Dickinson, M., & Pettini, M. 1999, ApJ, 519, 1

- Steidel, C. C., Kollmeier, J. A., Shapley, A. E., Churchill, C. W., Dickinson, M., & Pettini, M. 2002, *ApJ*, 570, 526
- Strickland, D. K. & Stevens, I. R. 2000, *MNRAS*, 314, 511
- Tytler, D., Boksenberg, A., Sargent, W.L.W., Young, P., & Kunth, D. 1987, *ApJS*, 64, 667
- Vogt, S. S., Allen, S. L., Bigelow, B. C., Bresee, L., Brown, B., Cantrall, T., Conrad, A., Coutoure, M., Delaney, C., Epps, H. W., et al. 1994, *Proc. SPIE*, 2198, 362

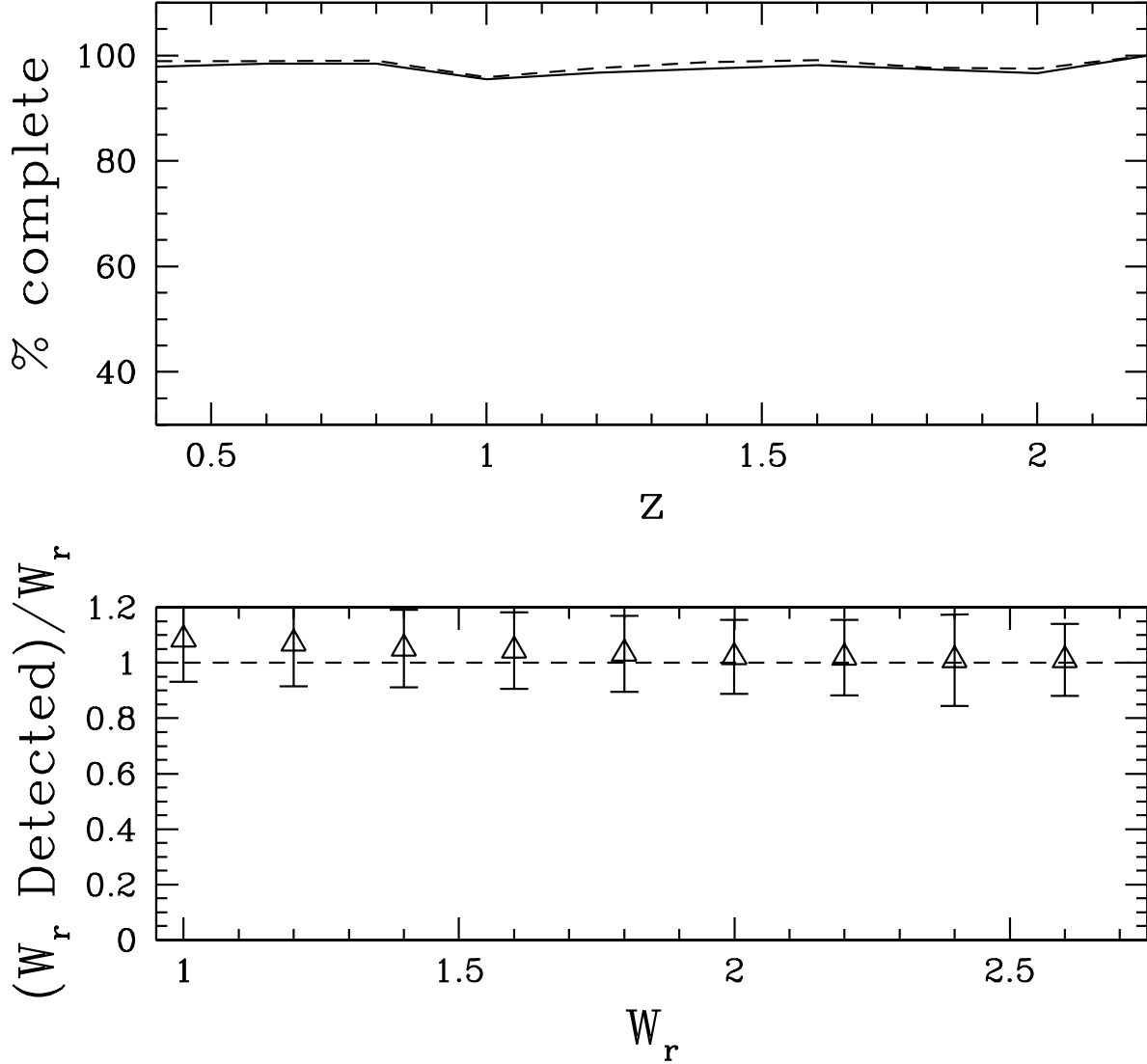


Fig. 1.— Completeness measurements for the automated SDSS-DR3 absorption search, based on Monte-Carlo simulations ($S/N > 7$). The top panel indicates percent completeness versus absorption redshift, with the solid line indicating systems of $W_r > 1.0 \text{ \AA}$ and the dashed line for systems of $W_r > 1.4 \text{ \AA}$. The bottom panel depicts the W_r measured by the automated search algorithm versus the actual W_r of the system added, with the vertical axis indicating the average ratio plus RMS error of systems for each 0.1 \AA W_r bin (the horizontal axis).

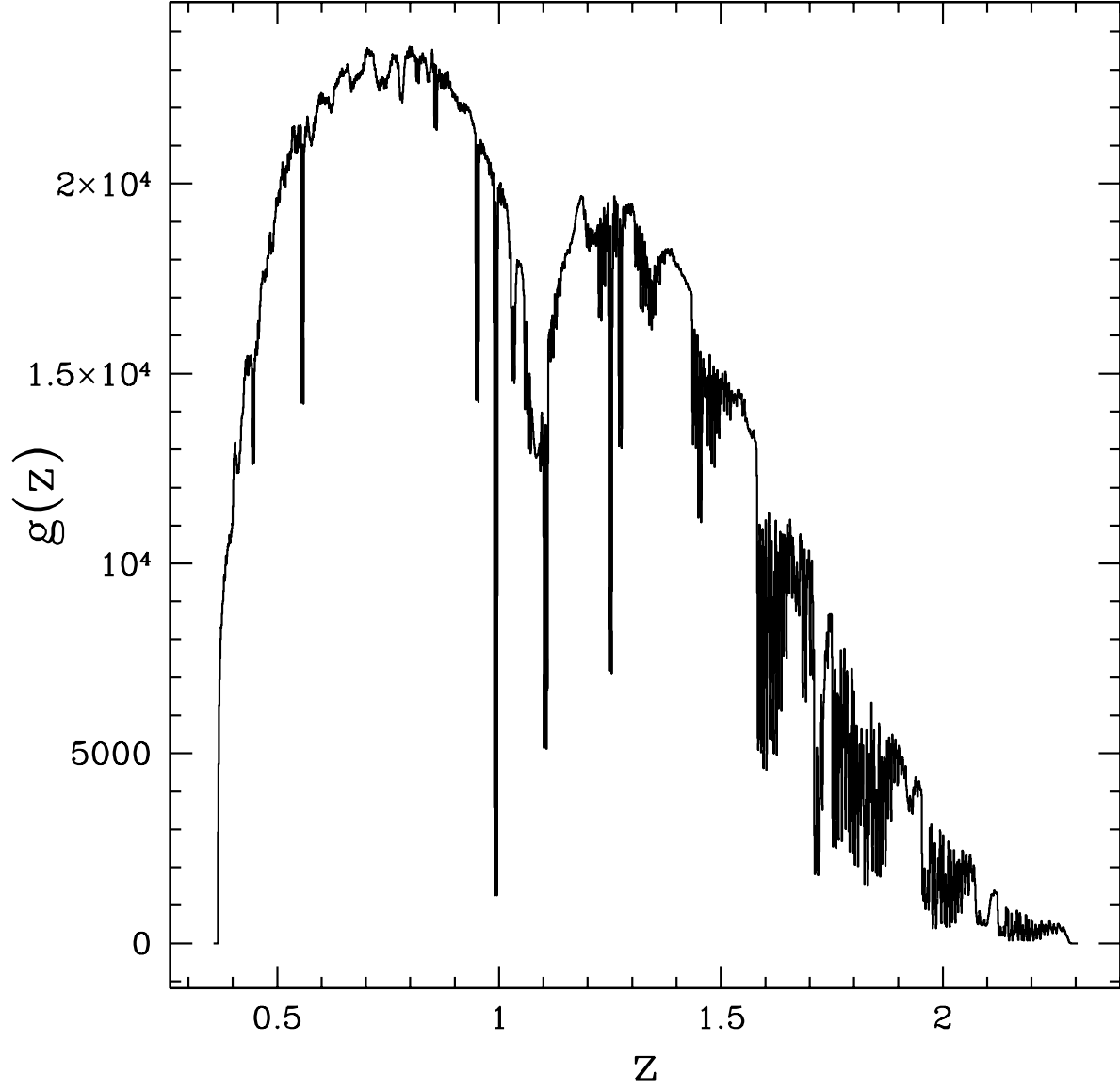


Fig. 2.— The redshift path density, $g(z)$, probed by SDSS-DR3. This represents the total number of lines of sight at a given redshift in which it is possible to detect a strong Mg II system in the SDSS-DR3 spectra. Clear in this plot are sky-absorption features at high redshift, as well as very strong lines at $z \sim 1$ at $z \sim 1.25$.

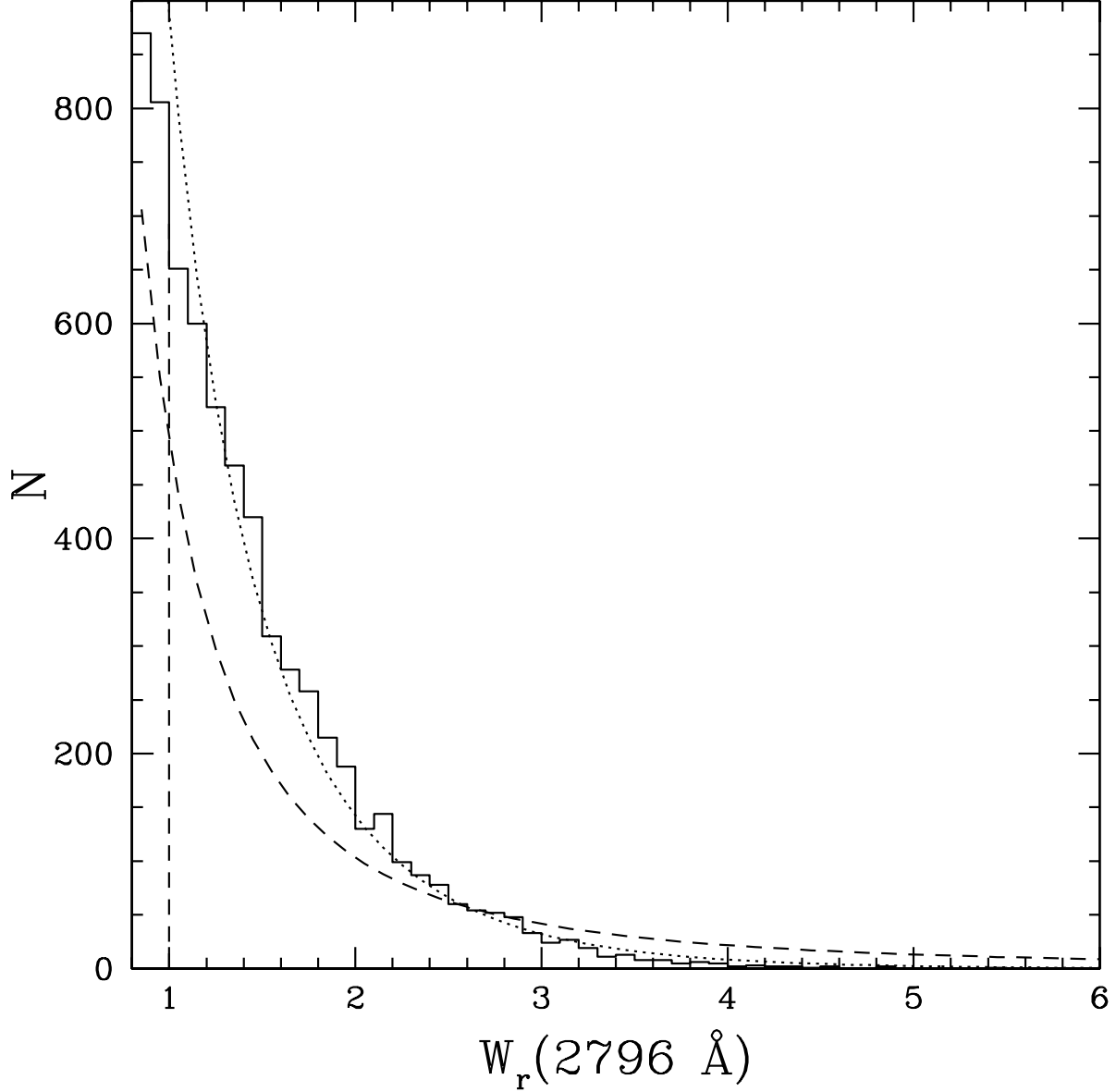


Fig. 3.— A histogram of the W_r values for the MgII systems discovered in SDSS-DR3 with our automated search algorithm. The vertical dashed line is located at $W_r = 1.0 \text{ \AA}$. Given that the incidence of W_r continues to rise well below 1 \AA , the survey is expected to be $> 95\%$ complete. A power law fit for systems of $W_r > 1.0 \text{ \AA}$ is plotted as a dashed line; $f(W_r) = 490.37W_r^{-2.245}$. The dotted line represents a modified Schechter functional fit the $W_r > 1.0 \text{ \AA}$ data, $f(W_r) = 2398.4W_r^{-1.19}e^{-W_r}$.

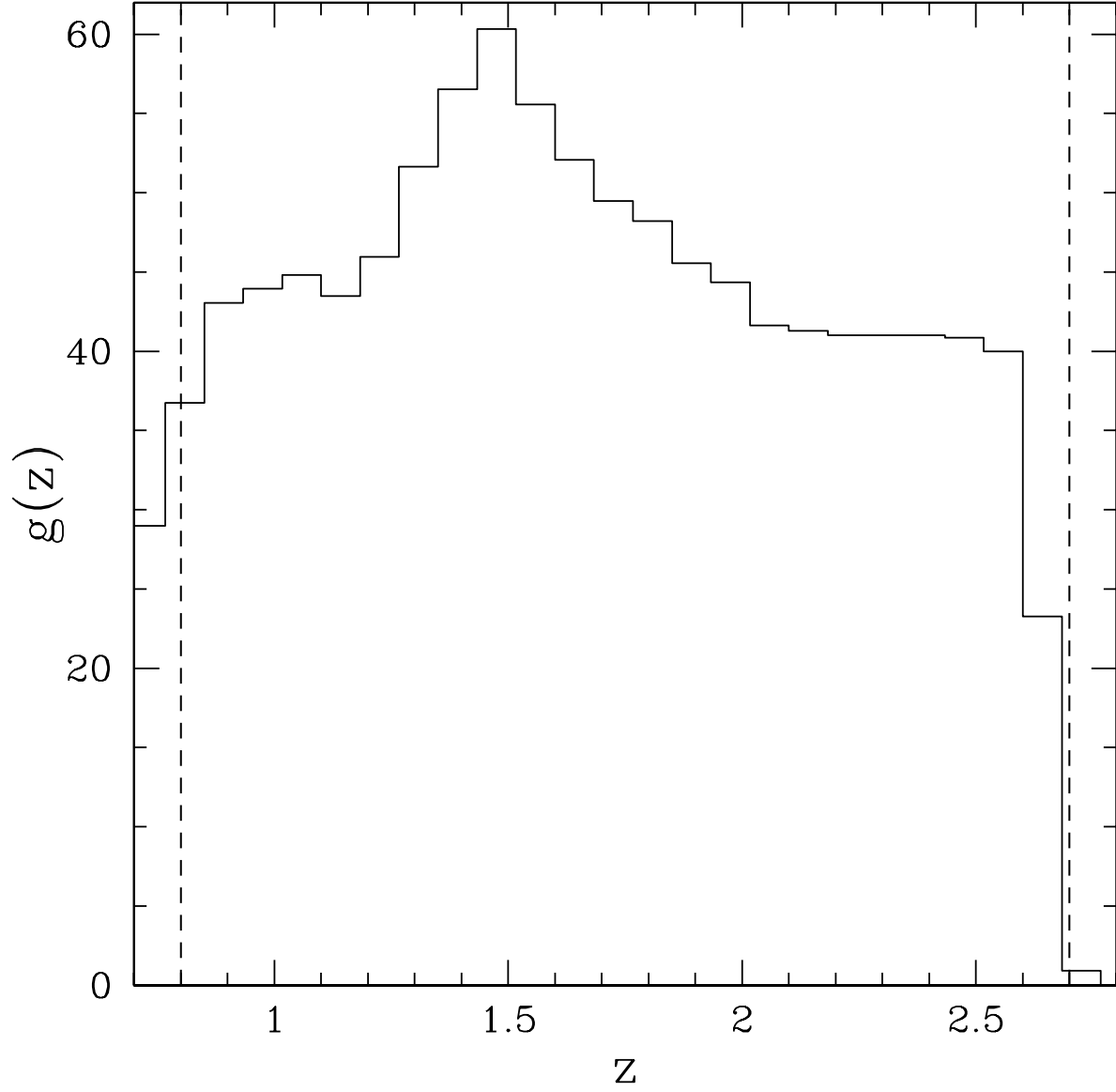


Fig. 4.— The redshift path density, $g(z)$, probed in the high resolution survey. The dashed vertical lines indicate the redshift region considered in the work presented in this paper.

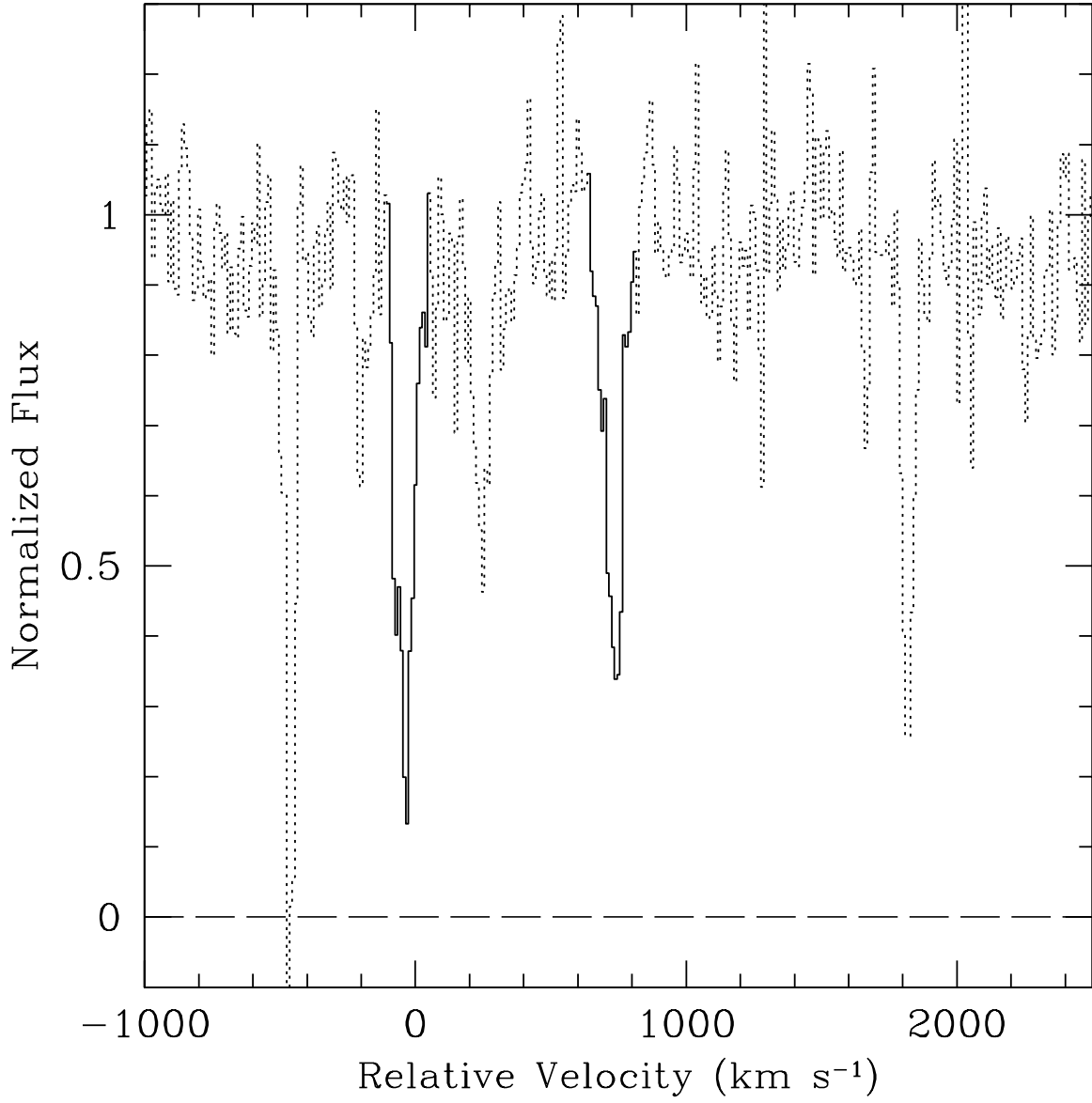


Fig. 5.— An example Mg II system discovered at $z = 2.51$ in the spectrum of Q1337+11. This system is located at $\sim 9800\text{\AA}$, where the sky begins to crowd the spectrum yet is easily identified at this spectral resolution and signal-to-noise.

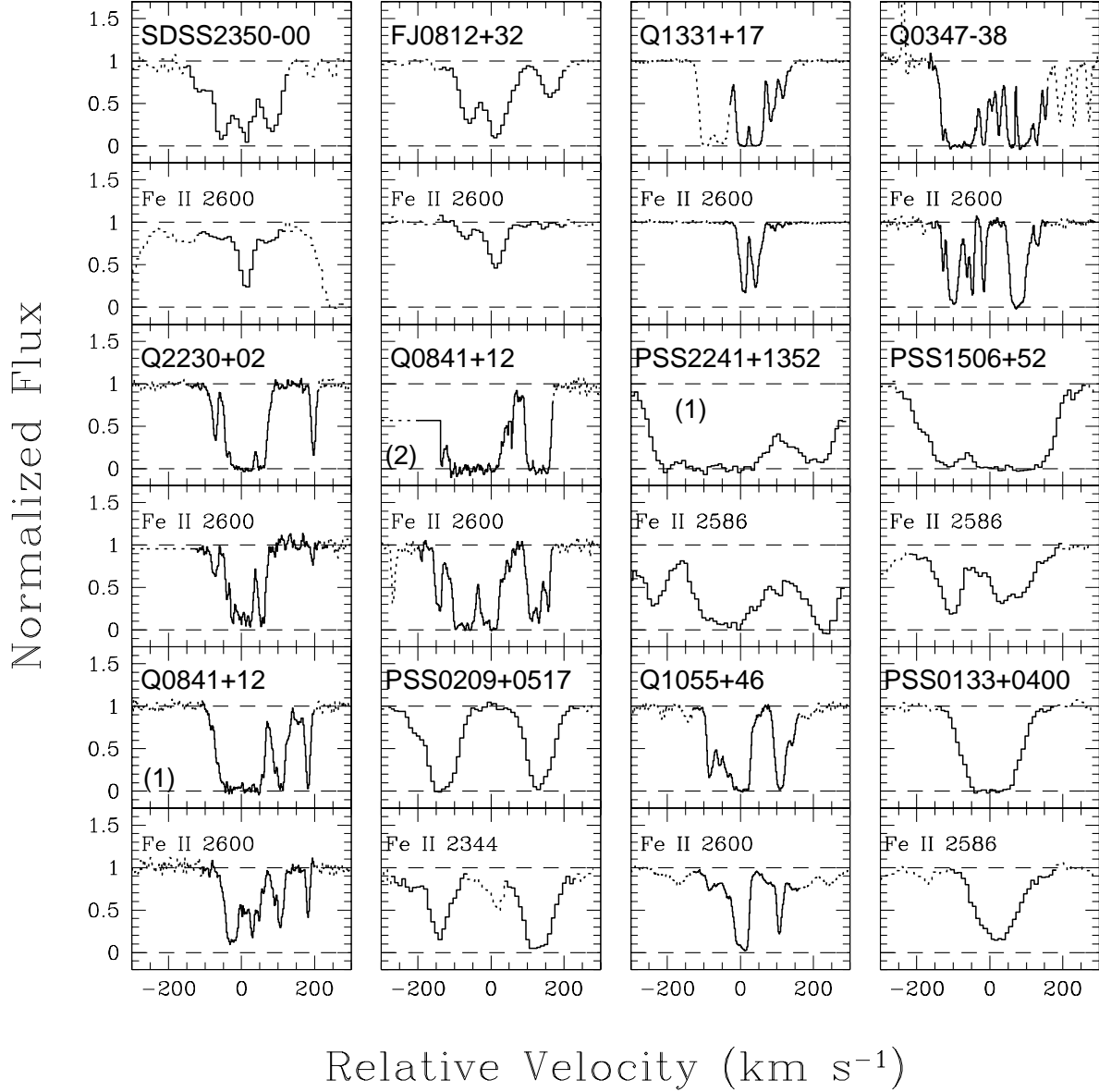
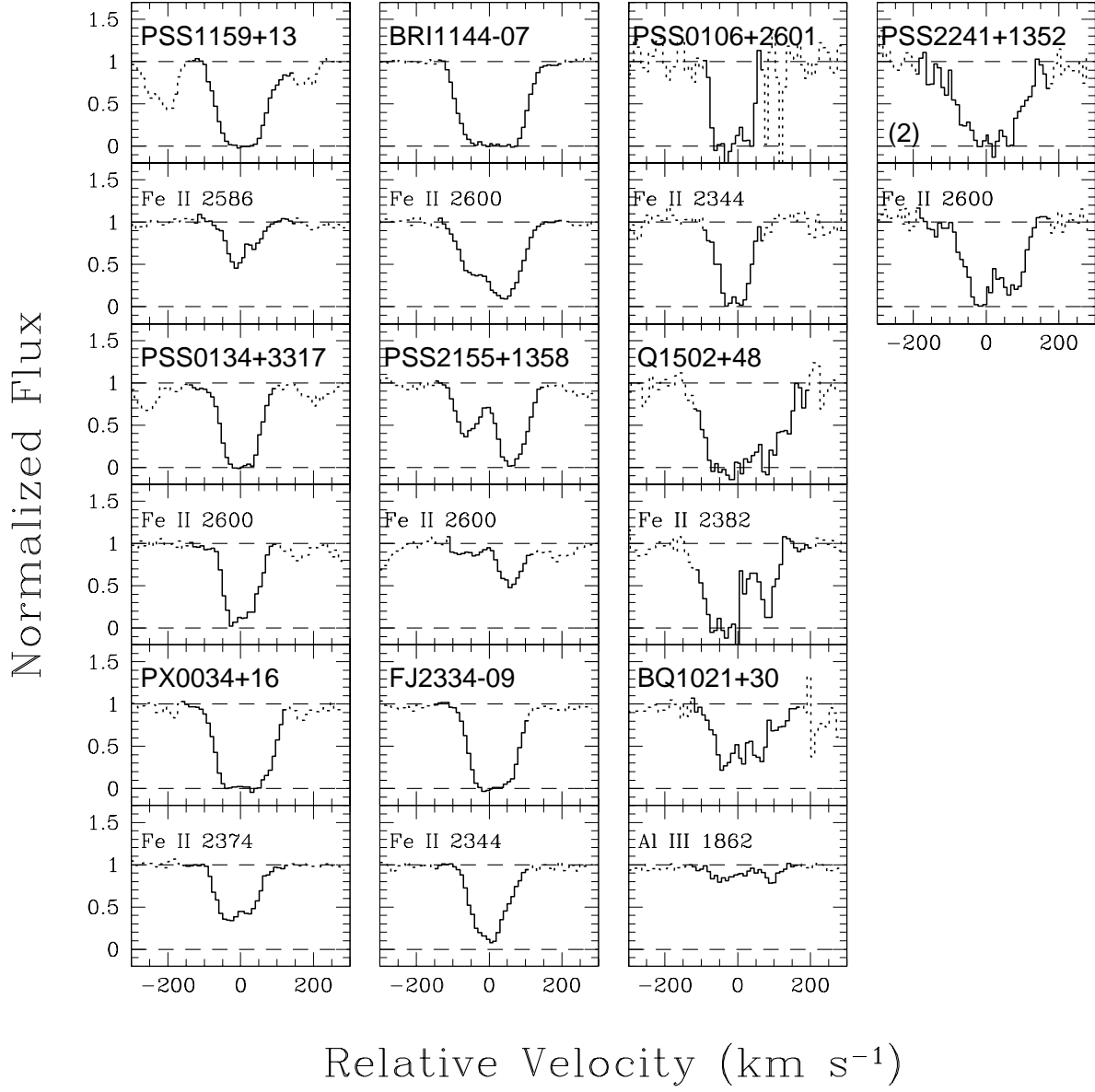


Fig. 6.— The 22 detected $W_r > 1.0 \text{ \AA}$, MgII absorption systems detected in the high resolution survey. For each system the MgII 2796 absorption line is displayed in relative velocity space with 0 km s^{-1} centered at the redshift reported in Table 2, with (1) referring to the low-z and (2) to the high-z system in cases of multiple detections per quasar. For each system, an associated, less saturated metal transition is displayed below the MgII 2796 feature. The systems are ordered by increasing redshift from top to bottom then left to right.



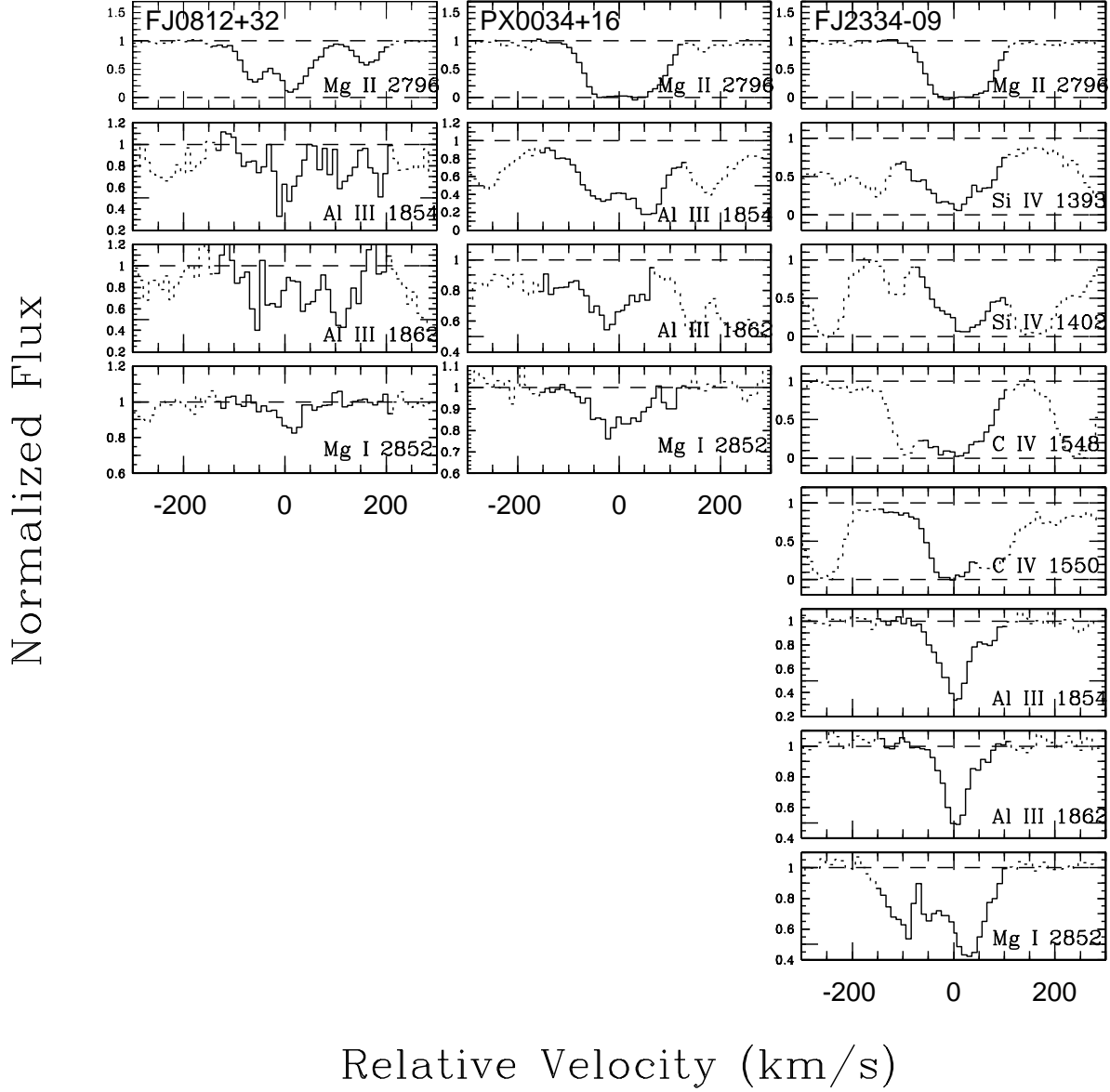
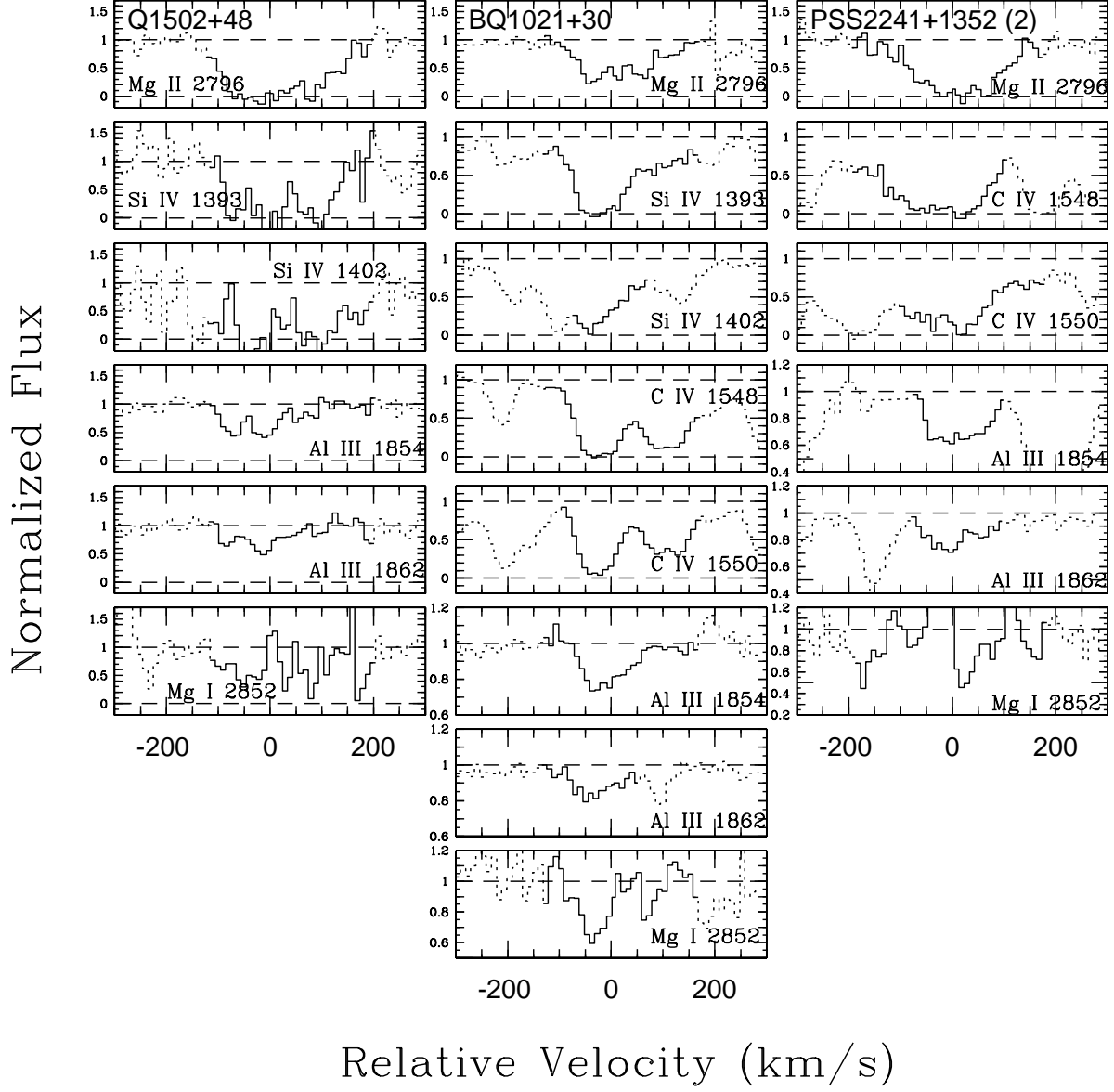


Fig. 7.— Six systems for which transitions of AlIII, CIV, and SiIV are detected. This figure adopts the same labeling as Figure 6.



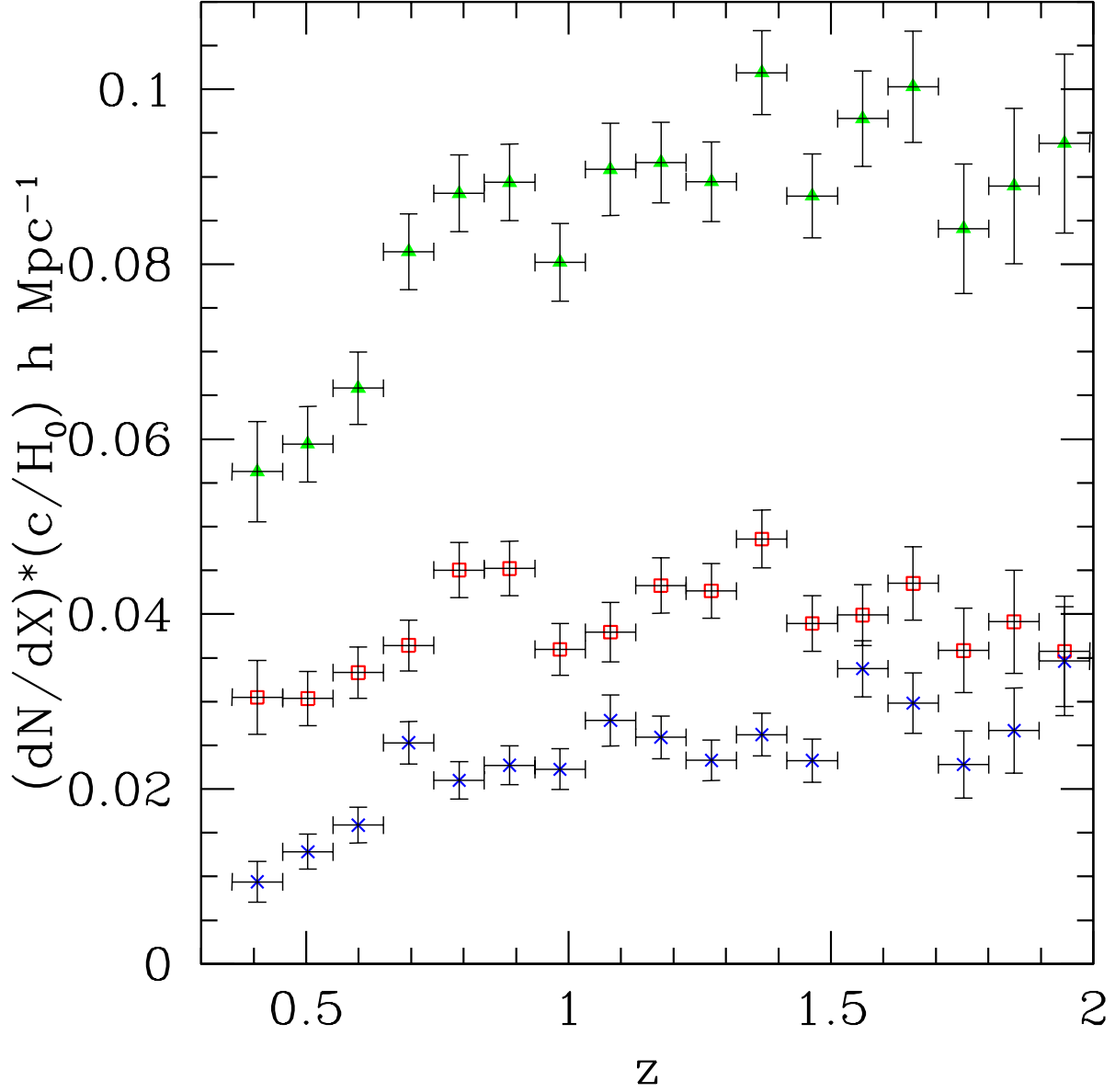


Fig. 8.— The incidence of strong Mg II absorbers, $\ell_{\text{Mg}}(X)$, from the SDSS-DR3 over the range $0.35 < z < 2$. The triangles show the full sample ($W_r > 1 \text{ \AA}$), the open squares are all systems of $1.0 \text{ \AA} < W_r < 1.4 \text{ \AA}$ and systems of $W_r > 1.8 \text{ \AA}$ are indicated with cross-hatches. The differences between the datasets in this plot have important implications for the nature of Mg II absorption hosts.

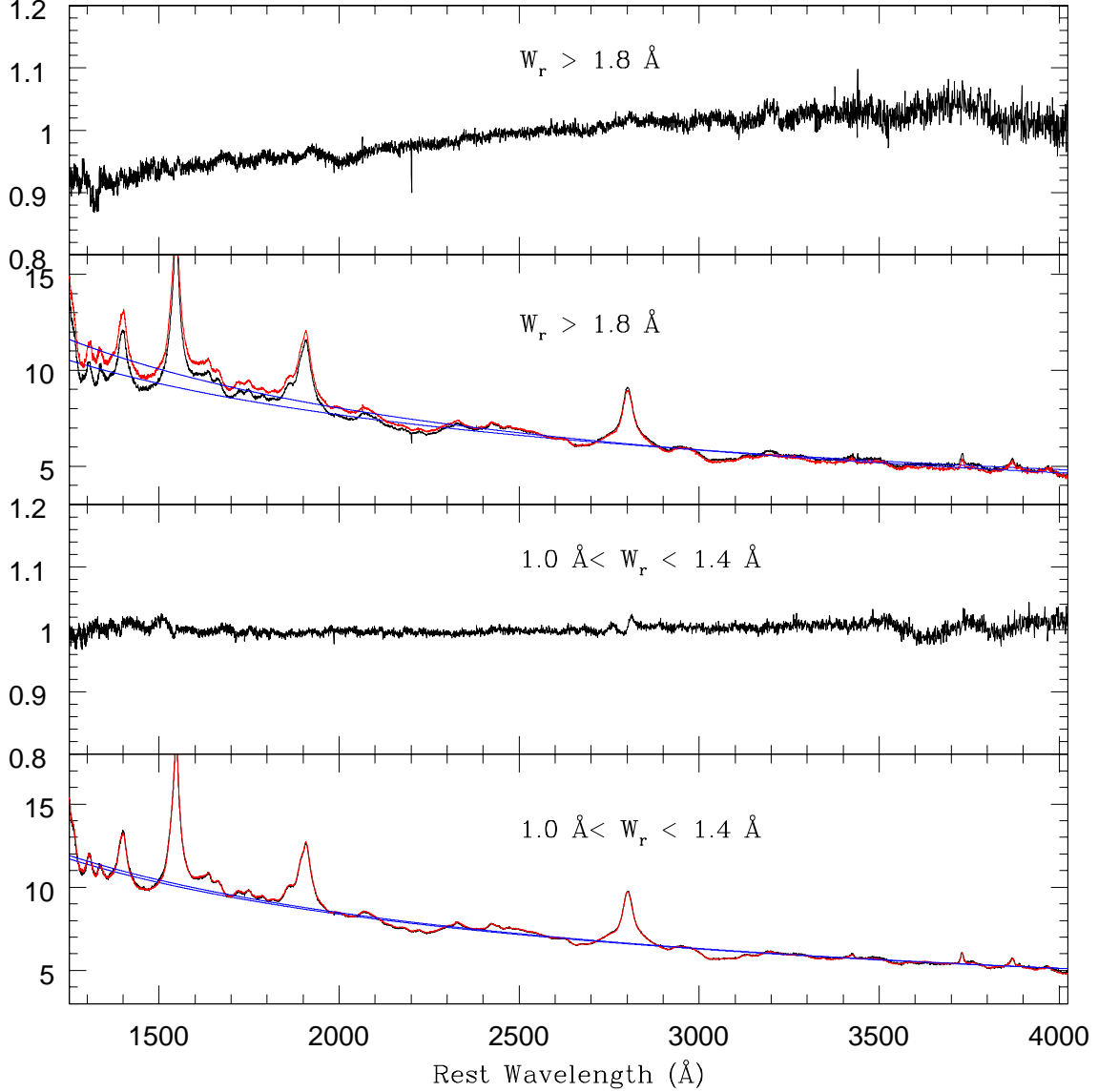


Fig. 9.— Results from an analysis of the dust reddening of quasar spectra hosting strong Mg II absorption. The top two panels are results from the $W_r > 1.8 \text{ \AA}$ systems with the lower panel displaying composite spectra of quasars hosting strong Mg II absorption (black) and quasars without absorption (red). The top panel is the absorption spectra divided by the non-absorption spectra. The bottom two panels are the equivalent results for systems of $1.0 \text{ \AA} < W_r < 1.4 \text{ \AA}$. These results are indicative of the spectra of those quasars hosting the largest of Mg II systems having been reddened.

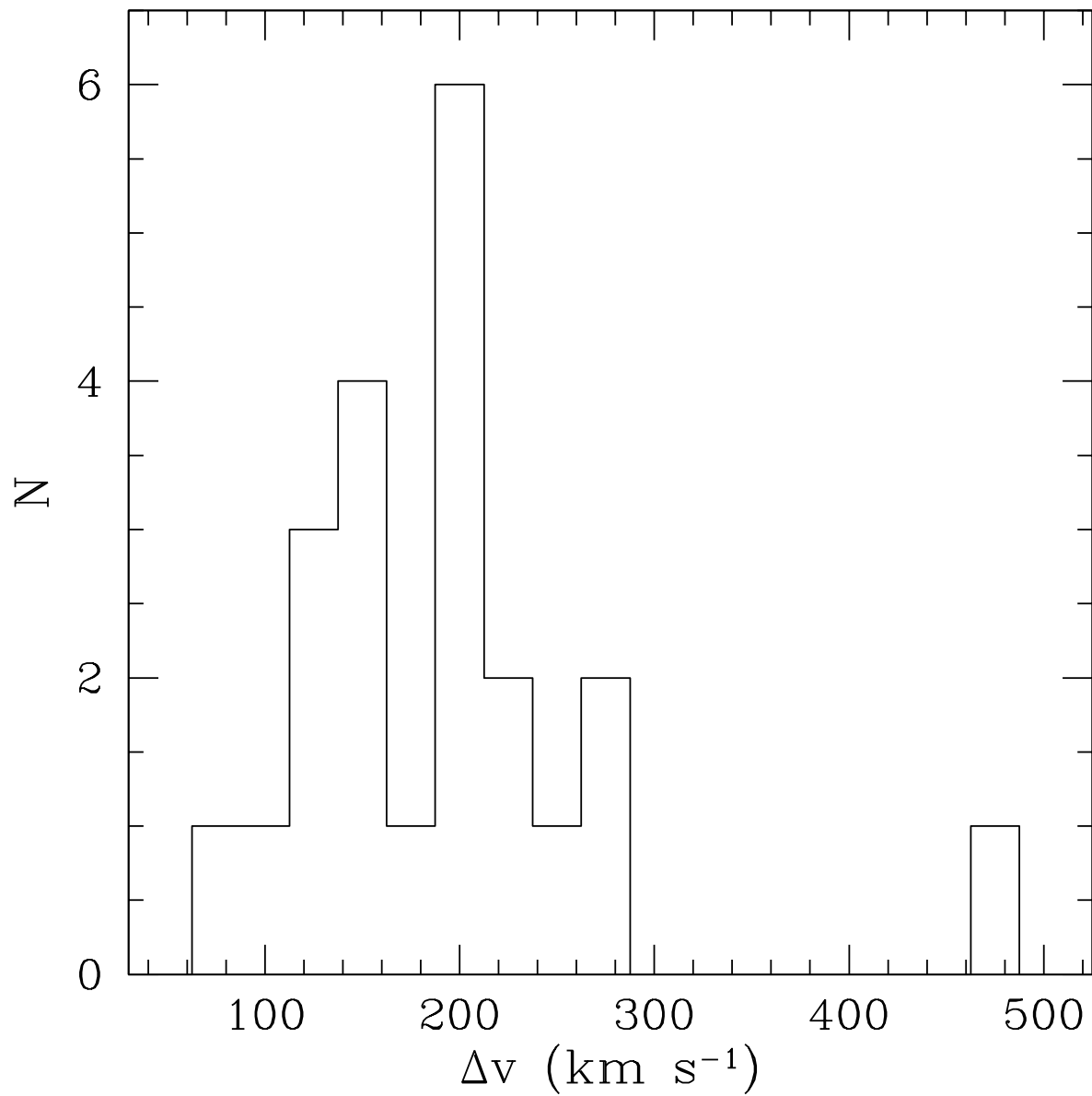


Fig. 10.— A histogram of Δv for the 22 systems discussed in this paper. Note the sharp cutoff at $\sim 100 \text{ km s}^{-1}$ corresponds to the $W_r > 1.0 \text{ \AA}$ limit imposed for consideration of a Mg II system. More importantly, note the near absence of systems with very large Δv value.

Table 1. SDSS-DR3 $W_r(2796) > 1.0 \text{ \AA}$ Mg II Systems

Quasar	RA	Dec	z_{qso}	$z_{Mg II}$	$W_r(2796)$
J000009.42-102751.87	00:00:09.42	-10:27:51.87	1.844	1.313	1.69
J000050.60-102155.87	00:00:50.60	-10:21:55.87	2.640	1.056	1.17
J000053.72+150637.20	00:00:53.72	+15:06:37.20	1.411	0.897	1.63
J000143.41+152021.49	00:01:43.41	+15:20:21.49	2.638	1.598	1.03
J000221.11+002149.46	00:02:21.11	+00:21:49.46	3.057	1.958	2.33
J000221.80+151454.58	00:02:21.80	+15:14:54.58	1.823	1.172	1.05
J000221.80+151454.58	00:02:21.80	+15:14:54.58	1.823	1.435	1.29
J000221.80+151454.58	00:02:21.80	+15:14:54.58	1.823	0.716	1.22
J000221.80+151454.58	00:02:21.80	+15:14:54.58	1.823	0.846	1.68
J000341.22-094101.03	00:03:41.22	-09:41:01.03	1.739	1.584	2.39

Note. — The complete version of this table is in the electronic edition of the Journal. The printed edition contains only a sample.

Table 2. High Resolution Survey Quasars and Found Mg II Systems

QSO	Inst	z_{qso}	z_{min}	z_{max}	$z_{Mg II}$	Δv	W_r	Metals	components
BR0019-15	1	4.53	1.40	1.98					
BR0951-04	1	4.37	1.36	2.00					
HS0741+47	1	3.22	0.81	1.67					
J0255+00	1	3.97	1.16	1.92					
PH957	1,2	2.69	0.47	2.76					
PSS0957+33	1,2	4.25	1.29	2.65					
PSS1443+27	1	4.41	1.38	2.12					
Q0000-26	1	4.11	1.26	1.91					
Q0149+33	1	2.43	0.46	1.33					
Q0201+11	1	3.61	1.01	1.73					
Q0201+36	1	2.49	0.69	1.57					
Q0249-22	1	3.20	0.30	0.80					
Q0322-32	1		0.42	0.92					
Q0336-01	1	3.20	0.80	1.28					
Q0347-38	1	3.23	0.84	1.62	1.457	216	2.237		7
Q0450-13	1	2.30	0.34	0.76					
Q0458-02	1	2.29	0.41	1.25					
Q0551-36	1	2.32	0.42	1.23					
Q0757+52	1		0.32	0.83					
Q0836+11	1	2.70	0.52	1.57					
Q0841+12	1	2.20	0.71	1.57	1.098	208	1.450		4
Q0841+12					1.219	274	2.388		5
Q0930+28	1	3.42	0.86	1.56					
Q0952-01	1	4.43	1.36	1.91					
Q1005+36	1		0.80	1.51					
Q1055+46	1	4.13	1.25	1.86	1.386	210	1.164		4
Q1104-18	1	2.31	0.44	1.47					
Q1108-07	1	3.92	1.12	1.98					
Q1202-07	1	4.69	1.49	2.00					
Q1210+17	1	2.54	0.56	1.21					
Q1215+33	1	2.61	0.39	1.26					

Table 2—Continued

QSO	Inst	z_{qso}	z_{min}	z_{max}	$z_{Mg II}$	Δv	W_r	Metals	components
Q1223+17	1	2.92	0.71	1.57					
Q1331+17	1	2.08	0.51	1.37	1.328	66	1.189		2
Q1346-03	1	3.99	1.18	1.98					
Q1425+60	1	3.17	0.81	1.21					
Q1759+75	1	3.05	1.14	1.71					
Q1850+40	1	2.12	0.82	1.79					
Q2038-01	1	2.78	0.65	1.21					
Q2206-19	1	2.56	0.52	1.33					
Q2223+20	1,2	3.56	0.99	2.65					
Q2230+02	1	2.51	0.38	1.46	1.059	110	1.234		4
Q2231-00	1	3.02	0.74	1.29					
Q2233+13	1	3.27	0.86	1.61					
Q2343+12	1	2.52	0.43	1.28					
Q2344+12	1	2.79	0.55	1.17					
Q2348-01	1	3.01	0.81	1.68					
Q2358-02	1		0.66	1.33					
BQ1021+30	2	3.12	0.73	2.65	2.329	200	1.023	SiIV,CIV,AIII	3
BRI1144-07	2	4.16	1.26	2.65	1.908	190	1.833		2
BRJ0426-2202	2	4.30	1.32	2.65					
CTQ460	2	3.13	0.68	2.65					
FJ0747+2739	2	4.11	1.25	2.65					
FJ0812+32	2	2.70	0.63	2.65	1.223	260	1.200		3
FJ0812+32					2.626	280	1.300	SiIV,CIV,AIII	1
FJ2129+00	2	2.94	0.72	2.65					
FJ2334-09	2	3.33	0.90	2.65	2.152	140	1.363	SiIV,CIV,AIII	1
HS1132+22	2	2.88	0.66	2.65					
HS1437+30	2	2.99	0.70	2.65					
PC0953+47	2	4.46	1.40	2.50					
PKS1354-17	2	3.15	0.79	2.65					
PSS0106+2601	2	4.32	1.32	2.65	2.198	130	1.110		1
PSS0133+0400	2	4.13	1.25	2.65	1.666	160	1.632		2

Table 2—Continued

QSO	Inst	z_{qso}	z_{min}	z_{max}	z_{MgII}	Δv	W_r	Metals	components
PSS0134+3317	2	4.52	1.40	2.65	1.757	130	1.145		1
PSS0209+0517	2	4.18	1.26	2.65	1.282	380	1.756		1
PSS0808+52	2	4.45	1.40	2.65					
PSS1159+13	2	4.07	1.22	2.65	1.739	130	1.386		2
PSS1248+31	2	4.35	1.32	2.65					
PSS1253-02	2	4.01	1.18	2.65					
PSS1315+29	2	4.18	1.29	2.65					
PSS1432+39	2	4.28	1.31	2.65					
PSS1506+52	2	4.18	1.25	2.65	1.472	280	3.407		2
PSS1723+2243	2	4.52	1.43	2.65					
PSS2155+1358	2	4.26	1.29	2.65	1.914	200	1.287		2
PSS2241+1352	2	4.44	1.32	2.65	1.339	470	4.626		2
PSS2241+1352					2.542	170	1.772		2
PSS2323+2758	2	4.18	1.25	2.65					
PSS2344+0342	2	4.30	1.29	2.65					
PX0034+16	2	4.29	1.32	2.65	1.800	160	1.576		2
Q0112-30	2	2.96	0.71	2.65					
Q0821+31	2	2.61	0.61	2.65	2.535	190	1.738	SiIV,CIV,AIII	2
Q0933+28	2		0.93	2.65					
Q1209+09	2	3.30	0.86	2.65	2.585	270	3.020	SiIV,CIV,AIII	2
Q1337+11	2	2.92	0.68	2.65					
Q1502+48	2	3.20	0.82	2.65	2.272	220	1.807	AIII	2
Q2342+34	2	3.01	0.77	2.65					
SDSS0127-00	2	4.06	1.22	2.65					
SDSS2350-00	2	3.01	0.75	2.65	0.863	200	1.474		3
SDSS2350-00					2.425	280	2.732	SiIV,CIV,AIII	2

Table 3. SDSS-DR3 Mg II dN/dX

$< z >$	dN/dX $W_r > 1.0 \text{ \AA}$	N	dN/dX $1.0 \text{ \AA} < W_r < 1.4 \text{ \AA}$	N	dN/dX $W_r > 1.8 \text{ \AA}$	N
0.41	0.056 ± 0.006	96	0.030 ± 0.004	52	0.009 ± 0.002	16
0.50	0.059 ± 0.004	190	0.030 ± 0.003	97	0.012 ± 0.002	41
0.60	0.066 ± 0.004	253	0.033 ± 0.003	128	0.016 ± 0.002	61
0.70	0.081 ± 0.004	351	0.036 ± 0.003	157	0.025 ± 0.002	109
0.79	0.088 ± 0.004	403	0.045 ± 0.003	206	0.021 ± 0.002	96
0.89	0.089 ± 0.004	417	0.045 ± 0.003	211	0.023 ± 0.002	106
0.98	0.080 ± 0.004	328	0.036 ± 0.003	147	0.022 ± 0.002	91
1.08	0.091 ± 0.005	297	0.038 ± 0.003	124	0.028 ± 0.003	91
1.18	0.092 ± 0.005	396	0.043 ± 0.003	187	0.026 ± 0.002	112
1.27	0.089 ± 0.004	388	0.043 ± 0.003	185	0.023 ± 0.002	101
1.37	0.102 ± 0.005	451	0.048 ± 0.003	215	0.026 ± 0.002	116
1.46	0.088 ± 0.005	336	0.039 ± 0.003	149	0.023 ± 0.002	89
1.56	0.097 ± 0.005	315	0.040 ± 0.003	130	0.034 ± 0.003	110
1.66	0.100 ± 0.006	249	0.044 ± 0.004	108	0.030 ± 0.003	74
1.75	0.084 ± 0.007	129	0.036 ± 0.005	55	0.023 ± 0.004	35
1.85	0.089 ± 0.009	100	0.039 ± 0.006	44	0.027 ± 0.005	30
1.94	0.094 ± 0.010	84	0.036 ± 0.006	32	0.035 ± 0.006	31
2.04	0.076 ± 0.013	33	0.016 ± 0.006	7	0.032 ± 0.009	14
2.14	0.070 ± 0.020	12	0.012 ± 0.008	2	0.029 ± 0.013	5
2.23	0.065 ± 0.024	7	0.046 ± 0.021	5	0.009 ± 0.009	1

Note. — All dN/dX values reported are multiplied by c/H_0 for ease of readability, and are in units of $h \text{ Mpc}^{-1}$.

Table 4. dN/dX and dN/dz Functional Fits to SDSS-DR3 Mg II Systems

$W_r(\text{\AA})$	Shape ^a	Normalization
$dN/dX = N + mz$		
> 1.0	0.022 ± 0.004	0.036 ± 0.004
> 1.8	0.011 ± 0.002	0.011 ± 0.002
$1.0 < W_r < 1.4$	0.002 ± 0.003	0.036 ± 0.002
$dN/dX = N \exp^{-z_0/z}$		
> 1.0	0.275 ± 0.05	0.113 ± 0.006
> 1.8	0.467 ± 0.10	0.037 ± 0.003
$1.0 < W_r < 1.4$	0.123 ± 0.07	0.044 ± 0.003
$dN/dX = N(1 + z)^\gamma$		
> 1.0	0.54 ± 0.10	0.06 ± 0.004
> 1.8	0.98 ± 0.154	0.01 ± 0.001
$1.0 < W_r < 1.4$	0.13 ± 0.15	0.04 ± 0.004
$dN/dz = N(1 + z)^\gamma$		
> 1.0	$1.40(1.24, 1.56)$	$0.08(0.095, 0.075)$
> 1.4	$1.74(1.52, 1.96)$	$0.036(0.042, 0.030)$
> 1.8	$1.92(1.60, 2.22)$	$0.016(0.021, 0.013)$
$1.0 < W_r < 1.4$	$0.99(0.77, 1.28)$	$0.051(0.060, 0.041)$
$1.4 < W_r < 1.8$	$1.56(1.25, 1.89)$	$0.020(0.025, 0.015)$
$m, z_0, \text{ or } \gamma$		

a

Note. — These are the 1σ errors for the minimized- χ^2 power-law fits and the 95% Confidence Limits for the maximum likelihood power-law fits to the SDSS-DR3 dN/dz data. For the dN/dz results, the upper and lower Confidence Limits for γ and N are presented in parentheses. The values of N for these fits are calculated by constraining the integral of $g(z) * dN/dz$ to equal the observed number of systems for a given cut in W_r .